# *Colloquium*: Quantum crystallizations of $^4$He in superfluid far from equilibrium

R. Nomura[*] and Y. Okuda[†]

*Department of Physics, Tokyo Institute of Technology, Tokyo 152-8551, Japan*

(published 2 December 2020)

Quantum crystallization of $^4$He is a first-order phase transition from a superfluid liquid and can proceed extremely quickly at particularly low temperatures. The entropy difference between the two quantum phases, the quantum crystal and superfluid liquid, is small and atoms are carried to the crystal surface via a dissipationless superflow. A limiting process of the transition near absolute zero temperature is quasiparticle scattering off the crystal surface, which is less frequent at lower temperatures. It is known that interfacial phenomena, such as crystallization wave propagations and total reflection of ultrasound, occur on $^4$He crystal surfaces as a result of the rapid crystallization. The rapid crystallization allows the fundamental physics of crystal shape and growth to be examined in a measurable timescale in laboratories, which otherwise cannot be observed in classical crystals. This Colloquium describes far from equilibrium phenomena of significantly deformed $^4$He quantum crystals when they are subjected to original driving forces, which are small and usually believed to be irrelevant for ordinary classical crystals. Using driving forces such as gravity, superflow, wettability, acoustic waves, container oscillations, and frictional forces, $^4$He crystals are placed under highly nonequilibrium conditions, showing various kinds of extraordinary crystallization and relaxation processes in a superfluid liquid. Rapid crystal shape deformations sometimes influence the surrounding superfluid field in return, resulting in instabilities of the flat crystal surface. Direct visualizations by a high-speed video camera are made, providing an unambiguous observation of the dynamics far from equilibrium of $^4$He quantum crystals at extremely low temperatures.

DOI: 10.1103/RevModPhys.92.041003

## CONTENTS

## I. INTRODUCTION

Crystal growth of classical materials usually proceeds extremely slowly. This is because the material and/or heat transport process to the crystal surface is slow due to the dissipation. Therefore, it is generally difficult to establish the minimum energy equilibrium shape of crystals. For example, a mineral crystal grows over a geological timescale and its macroscopic shape is usually not the equilibrium shape but rather a growth shape that reflects the anisotropy of the interface mobility and is quenched from the environment in which it has grown. Similarly, the shapes of snow crystals are determined by their growth conditions, and their growth history is recorded in their shape. This is why a snow crystal is referred to as a "letter from the sky" (Nakaya, 1954). In contrast, quantum mechanics allows a superfluid to exist near 0 K and $^4$He crystals grow from the superfluid rapidly due to the negligibly small dissipation. Consequently, quantum crystallization of $^4$He from the superfluid experiences a different limit. The shape of a $^4$He crystal can relax to the equilibrium shape rapidly and also can sensitively and instantaneously reflect the environmental conditions at the moment it forms. Such swift crystallization in return influences the superfluid field and thus the surface and
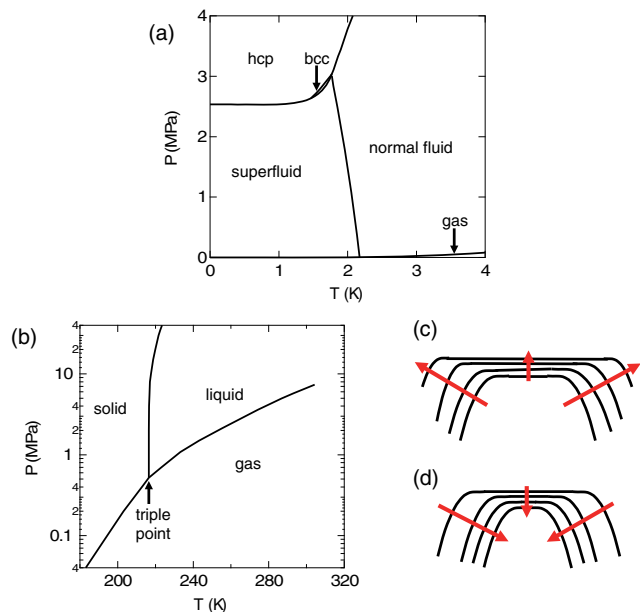
[*]nomura.r.aa@m.titech.ac.jp
[†]okuda_yu@cl.bb4u.ne.jp

FIG. 1. (a) Phase diagram of 4He. It does not have a triple point and the superfluid liquid phase exists down to $T = 0$ K. (b) Phase diagram of $CO_2$ as a typical example of the classical materials. It has a triple point at which gas, liquid, and solid phases coexist. Below this point, the liquid phase does not exist. (c) Illustration of the growth shape of a crystal in which the facet expands. (d) Illustration of the melting shape of a crystal in which the facet shrinks.

superfluid are closely coupled, giving rise to a variety of dynamical phenomena far from equilibrium.

Crystallization of 4He from superfluid liquid is a first-order phase transition that takes place down to 0 K; see Fig. 1(a). It can advance rapidly because some of the transport processes in bulk phases proceed without dissipation in this system. The entropy difference between the quantum solid and liquid phases becomes extremely small at sufficiently low temperatures, resulting in negligible transport of released latent heat. 4He atoms are carried to the crystal surface during the growth by swift superflow without any dissipation. Impurities of other atomic species are removed to the container wall at cryogenic temperatures and do not hinder the crystallization process. In this superclean system, quasiparticle scattering off the crystal surface can limit the crystallization rate. The density of quasiparticles decreases with cooling and accordingly the crystallization proceeds more rapidly at lower temperatures (Andreev and Parshin, 1978; Lipson and Polturak, 1987; Balibar and Nozières, 1994; Balibar, Alles, and Parshin, 2005; Okuda and Nomura, 2008; Tsymbalenko, 2015). Rapid crystallization allows the fundamental physics of crystal shape and growth to be explored, which cannot be similarly examined for classical crystals due to their slow response. The rapid crystallization also means that the crystals can sensitively and quickly respond to weak driving forces such as gravity, superflow, wettability, acoustic waves, container oscillations, and frictional forces, which are believed to be irrelevant for ordinary classical crystals and typically neglected. 4He quantum crystals are a model system for

studying peculiar out-of-equilibrium phenomena which cannot be observed in classical systems due to the severe dissipation.

Using the previously mentioned novel driving forces, various kinds of extraordinary crystallization dynamics of 4He in superfluids have been discovered. Crystals have been strongly deformed and thus in highly nonequilibrium states even under weak driving forces, and the following relaxation has been observed. For studies of the dynamics out of equilibrium, direct visualization by a high-speed video camera has been helpful and is often essential for making definite observations.

This Colloquium is structured as follows. We begin with an explanation of the crystallization of 4He in superfluid liquids in Sec. II. In Secs. III and IV, we address the relaxation to an equilibrium crystal shape and the ripening process of 4He crystals, realized under zero gravity produced by the parabolic flight of a small jet plane. Next we describe experiments under gravity on the ground to explain the shape of falling crystals in superfluid liquids (Sec. V), rising superfluid droplets formed in a host crystal (Sec. VI), and anomalous asymmetric behavior in melting and growth after manipulation by acoustic radiation pressure (Sec. VII). Several novel surface phenomena of 4He crystals are also described, such as instabilities on 4He crystal surfaces in superfluid liquid (Sec. VIII), and the transverse motion of a 4He crystal on an asymmetrically oscillating horizontal plate (Sec. IX). Additional images and videos are provided as Supplemental Material.

## II. PROPERTIES OF 4He QUANTUM CRYSTALS

### A. Phase diagram and roughening transitions

At ordinary pressure and temperature $(P, T)$, the phase diagram of classical materials exhibits a triple point at which gas, liquid, and solid phases coexist. As a typical example, the phase diagram of $CO_2$ is shown in Fig. 1(b) (Martin Trusler, 2011). The triple point is at 5.2 bar and 217 K, below which the liquid phase does not exist. Crystals grow from the melt above this point, while they grow from the vapor below it. This is common in many of the classical materials.

However, 4He does not exhibit a triple point and the superfluid liquid phase exists down to $T = 0$ K without crystallization at low pressures as shown in Fig. 1(a). The crystal phase is not energetically favored because the attractive interaction of 4He atoms is weak compared to the zero-point energy of light atoms. Therefore, the superfluid liquid can exist at $T = 0$ K at low pressures and the crystal phase only appears at pressures higher than $P_0 = 25.3$ bar (Wilks, 1967). The crystallization pressure $P_0(T)$ is nearly temperature independent at low temperatures due to the small entropy difference between the two phases, superfluid and crystal. $P_0$ has a shallow minimum at 0.8 K because the velocity of transverse phonons in the crystal is lower than that of the longitudinal phonons in the superfluid, resulting in a slightly larger entropy of the crystal phase. The crystal structure of 4He is a hexagonal-close-packed (hcp) structure at $P_0$, but a small

pocket of body-centered-cubic (bcc) appears between 1.46 and 1.76 K. $^4$He atoms in the crystal have a large zero-point motion and exchange their positions via quantum tunneling at the frequency of the order of $10^7$ Hz, forming quantum crystals or quantum solids, where anomalous properties such as supersolidity have been proposed (Andreev and Lifshitz, 1969; Chester, 1970; Leggett, 1970).

The equilibrium crystal shape (ECS) is the shape that minimizes the total surface free energy. Determining the ECS is a basic problem in both the physics of real crystal shapes and general statistical mechanics. The roughening transition is a phase transition of the ECS (Burton, Cabrera, and Frank, 1951) and has been studied extensively in hcp $^4$He crystals. It is a transition between flat surfaces (or facets) and microscopically rough surfaces. The roughening transition of the (0001) plane or $c$ facet has been studied in detail (Balibar and Castaing, 1980; Balibar, Alles, and Parshin, 2005) and its transition temperature is $T_{R1} = 1.30$ K. The roughening transition has been theoretically described as an infinite-order phase transition belonging to the Berezinskii-Kosterlitz-Thouless (BKT) universality class. This theory has proven to be correct based on experiments confirming the expected universal behaviors of BKT transitions, such as a gradual increase in the step free energy on the $c$ facet with cooling, $\beta \propto \exp\{-\mathrm{const}/\sqrt{T_{R1} - T}\}$ (Wolf *et al.*, 1985; Gallet, Balibar, and Rolley, 1987). Thus, the roughening transition in $^4$He crystals is a demonstration of BKT transitions, as was the two-dimensional superfluid transition in $^4$He films (Kagiwada *et al.*, 1969; Kosterlitz and Thouless, 1973; Nelson and Kosterlitz, 1977; Bishop and Reppy, 1978). Two other roughening transitions of the $(10\bar{1}0)$ and $(10\bar{1}1)$ planes are known to exist, called the $a$ facet and $s$ facet, respectively (Avron *et al.*, 1980; Wolf, Balibar, and Gallet, 1983). Their transition temperatures are less accurately known but are believed to be $T_{R2} \approx 1.0$ K and $T_{R3} \approx 0.4$ K.

Higher-order facets, predicted by Landau for classical solids with long-range atomic interactions (Landau, 1965), are not observed in the equilibrium shape in $^4$He crystals but have been identified in the growth shapes (Todoshchenko *et al.*, 2008). In general, in both $^4$He and classical crystals clear, easily identified facets appear in the growth shapes. Rough surfaces grow faster than facets, so rough surfaces catch up with facets during crystal growth. As the growth progresses, the facet regions expand and the rough regions shrink as illustrated in Fig. 1(c) (Elbaum and Wettlaufer, 1993; Maruyama *et al.*, 2000), and hence crystal surfaces are often found to be completely covered by facets in growth shapes. On the contrary, melting shapes are often covered by rounded rough surfaces as in Fig. 1(d).

### B. Crystal growth

To drive the crystallization of $^4$He, a chemical potential difference between the crystal and superfluid liquid $\Delta\mu$ (per unit mass) has to be applied. Since $P_0$ is temperature independent at low enough temperatures, an overpressure from $P_0$ is a typical driving force and hence the chemical potential difference is expressed as

$$\Delta\mu = \frac{\Delta\rho}{\rho_C \rho_L}(P - P_0). \tag{1}$$

Here $\rho_C = 0.191$ g/cm$^3$ and $\rho_L = 0.172$ g/cm$^3$ are the respective densities of the crystal and the liquid and $\Delta\rho = \rho_C - \rho_L$. Under this driving, the rough crystal surface proceeds at a velocity $v$, and the crystal growth rate or the interface mobility $K$ at $T$ is defined by

$$v = K(T)\Delta\mu, \tag{2}$$

while the faceted crystal surface proceeds nonlinearly due to the motion of existing steps or to the nucleation of steps. A process that limits the crystal growth is the collision between the crystal surface and quasiparticles in the solid and liquid, which causes dissipation for the crystallization process (Bowley and Edwards, 1983; Nozières and Uwaha, 1987). For example, $K(T)$ of the rough surface is given as

$$K(T)^{-1} = A + BT^4 + C\exp\left(\frac{-\Delta}{k_B T}\right), \tag{3}$$

where the second and third terms are the contributions from collisions with phonons and rotons, respectively. The first term comes from imperfections in the crystal. $K(T)$ becomes extremely large at low temperatures for good quality crystals, leading to the emergence of intriguing interfacial phenomena of the quantum crystals.

First-order phase transitions are generally triggered by the nucleation of a new phase seed, arising from thermal or quantum fluctuations in a metastable phase protected by an energy barrier originating from the interfacial energy. At high temperatures the nucleation is usually via thermal activation, whereas at low temperatures quantum nucleation via macroscopic quantum tunneling becomes prominent. Efforts have been made to observe quantum nucleation of $^4$He crystals in a metastable superfluid liquid above $P_0$ (Tsymbalenko, 1992; Ruutu, Hakonen, Penttilä *et al.*, 1996; Sasaki and Mizusaki, 1998; Chavanne, Balibar, and Caupin, 2001; Ishiguro, Caupin, and Balibar, 2006; Nomura *et al.*, 2011; Matsuda *et al.*, 2013).

Finally, what is predicted in the extreme nonequilibrium condition is explained. The circumstance where crystallization or melting proceeds at sound velocity is a fundamental issue of interest (Leggett, 2003). Crystallization and melting are transitions between two phases with and without off-diagonal long-range order. Therefore, a novel state, such as a state with broken translational symmetry and off-diagonal long-range order, could emerge in the transient process, which is a kind of supersolid state realized only in nonequilibrium. While there have been several reports on the fast crystallization of $^4$He crystals by high driving (Graf and Maris, 1987; Ruutu, Hakonen, Babkin *et al.*, 1996; Tsymbalenko, 2000; Balibar, Chavanne, and Caupin, 2003; Nomura *et al.*, 2008), these crystallizations are still not fast enough to experimentally address the problem.

### C. Crystallization waves

It has been predicted that a unique wave on a $^4$He crystal surface should propagate via periodic melting and growth at

low temperatures, as if the surface were a free surface of a liquid (Andreev and Parshin, 1978). This is called a crystallization wave and was subsequently observed experimentally (Keshishev, Parshin, and Babkin, 1979, 1981). This is a good example of the coupling of the surface and superfluid mentioned in Sec. I. It was demonstrated that measurements of the dispersion relation and the damping could obtain accurate values of $K(T)$ and $\alpha$, where $\alpha$ is the surface tension or the surface free energy density. The anisotropic properties of the crystallization waves were investigated on vicinal surfaces, which are slightly inclined surfaces from the facet (Rolley *et al.*, 1994; Rolley *et al.*, 1995), providing a characteristic orientation dependence of the surface stiffness $\gamma$, which is defined by adding the second derivative by the angle to $\alpha$ as $\gamma = \alpha + \partial^2\alpha/\partial\phi^2$. Here $\phi$ is the angle from the facet. This orientation dependence should be a universal property of crystals (Nozières, 1992), but this is difficult to prove even qualitatively in classical crystals.

The fast rate of growth of $^4$He quantum crystals allows their responses and relaxations to be studied at convenient timescales, making them good systems for studying the fundamental and general physics of crystal shapes and growth, though it is interesting that peculiar phenomena, such as crystallization waves, can be used to reveal the basic aspects of crystal surface physics.

### D. Acoustic wave effects

Ultrasound measurements play a major role in studying $^4$He crystal surfaces in superfluid liquids. When a longitudinal ultrasound was injected onto a rough $^4$He crystal surface at low enough temperature, it was anomalously reflected by the surface. This is because melting and growth were induced by the pressure oscillation of the ultrasound $\delta p$, even at high frequency, and prevented the ultrasound from passing through the surface (Castaing and Nozières, 1980). Measuring the reflection or transmission coefficient of the ultrasound could determine $K(T)$ (Castaing, Balibar, and Laroche, 1980; Graf and Maris, 1987). In the low temperature limit, the rough crystal surface reflected the ultrasound almost totally. In later experiments, extremely high frequency ultrasounds were found to be slightly transmitted through a surface at particularly low temperatures (Poitrenaud and Legros, 1989; Amrit, Legros, and Poitrenaud, 1995). This transmission was caused by surface inertia, which is an intrinsic interface property associated with the kinetic energy of a moving interface (Kosevich and Kosevich, 1981; Uwaha and Nozières, 1985).

When an acoustic wave hits the surface of an object, the oscillating hydrostatic pressure $\delta p$ exerts no net force on the surface in the first order, because the time average of $\delta p$ vanishes $\overline{\delta p} = 0$. Here we suppose for simplicity that the surface is a complete absorber of the acoustic wave with no reflection or transition and that anharmonicity of the medium is neglected. Another source of force acting on the surface comes from the momentum flux density $(\rho u)u$, where $\rho$ and $u$ are the density and oscillation velocity of the medium (Sato and Fujii, 2001). The time average of the momentum flux density $\overline{\rho u^2}$ does not vanish and acts as a unidirectional force on the surface, although it appears strange that the oscillatory

motion of the medium transfers a nonzero net momentum to the surface. This acoustic stress on the surface is called acoustic radiation pressure and is a small force, usually much smaller than $\delta p$ (Rayleigh, 1902; Brillouin, 1925). Since $\overline{\rho u^2}$ is essentially the acoustic energy density, the acoustic radiation pressure can be expressed equivalently in terms of the pressure oscillation and is shown to be proportional to $\overline{\delta p^2}/\rho c^2$, where $c$ is the sound velocity (Borgnis, 1953). The acoustic radiation pressure is a second-order acoustic effect, present even without anharmonicity.

In the case of a surface with a finite reflection coefficient Re, the acoustic radiation pressure can be generally expressed as (Borgnis, 1953)

$$p = \frac{\overline{\delta p^2}}{\rho_1 c_1^2}\left\{1 - \frac{c_1}{c_2} + \mathrm{Re}^2\left(1 + \frac{c_1}{c_2}\right)\right\}. \quad (4)$$

Here the acoustic wave is injected from medium 1 to medium 2, and $\rho$ and $c$ are the density and sound velocity of each medium. For a $^4$He crystal in a superfluid liquid at low enough temperatures, Re $\approx 1$.

While acoustic radiation pressure can be used to control an object acoustically (Hoshi, Ochiai, and Rekimoto, 2014; Marzo *et al.*, 2015), it was not known whether it can induce a first-order phase transition. However, recently it was demonstrated that acoustic radiation pressure does induce both crystallization and melting of $^4$He crystals in superfluid below about 0.5 K due to their high interface mobility (Nomura *et al.*, 2003, 2004). Melting of the crystal, lowering the interface, was induced when an acoustic wave was applied downward on the crystal-superfluid interface from the superfluid side. Crystallization, lifting the interface, was induced when the acoustic wave was applied upward from the crystal side. Accordingly, acoustic waves can be used to manipulate the crystal-superfluid interface of the specified orientation and to examine the subsequent relaxation process, as in Sec. VII. Furthermore, peculiar acoustic effects, such as the fast growth of a $c$ facet and a reversal of acoustic radiation pressure above 0.5 K, have been detailed previously (Parshin and Tsymbalenko, 2003; Abe *et al.*, 2006; Okuda and Nomura, 2008).

### E. Instabilities

Owing to the high mobility of the crystal-superfluid interface in $^4$He, several kinds of hydrodynamic instability that are usually observable only on a liquid surface are expected to be realized on $^4$He crystal surfaces. For example, Faraday instability is a parametric excitation of surface waves on a liquid and was predicted to also occur on crystal surfaces as a parametric excitation of crystallization waves by van Saarloos and Weeks (1995). Kelvin-Helmholtz instability is induced by a shear flow along a liquid surface and was predicted to develop on rough surfaces of $^4$He crystals by Parshin (1985), Kagan (1986), and Uwaha and Nozières (1986).

Maksimov and Tsymbalenko (2002) reported on the instability of a crystal surface induced by a superflow produced by electron injection from a tungsten needle. This instability may

be explained as being Kelvin-Helmholtz instability or being due to the inhomogeneity of the superflow.

Bodensohn, Nicolai, and Leiderer (1986) reported the emergence of grooves on a flat crystal surface after a rapid temperature quench. This is believed to be due to a mechanical instability called Grinfeld instability (Grinfeld, 1986, 1993), which was systematically studied later by applying a controlled uniaxial stress on a $^4$He crystal (Torii and Balibar, 1992).

## III. RELAXATION TO EQUILIBRIUM CRYSTAL SHAPE OF $^4$He UNDER ZERO GRAVITY

When a $^4$He crystal much larger than a capillary length of 1 mm is contained in a large enough sample cell under gravity of $1g = 9.8$ m/s$^2$ it sinks in the superfluid liquid, with a horizontal interface separating the two phases to minimize the gravitational energy. The capillary length is given as $l_c = \sqrt{\alpha/\Delta\rho g}$, and gravity (surface free energy) dominates the overall energy of the system above (below) the scale of $l_c$ (de Gennes, Brochard-Wyart, and Quéré, 2004). In a zero-gravity environment produced by a parabolic flight, $l_c$ is divergently large and a $^4$He crystal on the order of 10 mm has been demonstrated to relax quickly to the ECS, which minimizes the total surface free energy. Once the ECS of the large crystal is obtained, which can be realized only under zero gravity, we can analyze the crystal shape from the microscopic step-step interactions and extract the surface free energy of the higher-order facets relative to that of the $c$ facet.

### A. Experimental setup

Investigating a gravity-free crystal shape of $^4$He requires one to conduct experiments in a new kind of multiple extreme condition, namely, ultralow temperature under reduced gravity. To achieve this condition, we developed a compact $^3$He-$^4$He dilution refrigerator that can be operated on a small jet plane (Takahashi *et al.*, 2015; Takahashi, Nomura, and Okuda, 2016). When the jet plane takes a specific trajectory, known as parabolic flight, at the top of the parabolic trajectory it provides a zero-gravity environment. The small jet plane used for the experiment was an MU-300, operated by Diamond Air Service in cooperation with the Japan Aerospace Exploration Agency (JAXA) ground-based program. The minimum gravity attained in the present parabolic flight was less than $0.01g$, which was small enough for our experimental purposes and thus is referred to as zero gravity in this Colloquium. The zero-gravity period continued for 20 s during the parabolic flight. Seven or eight parabolic flights were performed during each flight for a total flight time of about 2 h. A video clip movieZeroG is provided in the Supplemental Material (161) to demonstrate the experiment on the airplane.

The experiments on the small jet plane had restrictions on the total equipment weight, experimental space, experimental time, and electric power available. A compact $^3$He-$^4$He dilution refrigerator was specially designed to cool $^4$He crystals to ultralow temperatures. A small Gifford-McMahon refrigerator provided a 4-K stage in a vacuum chamber. A small volume $^4$He bath (8 l) connected to the 4-K stage served liquid $^4$He to a 1-K pot. The 1-K pot was installed below the 4-K stage and supplied
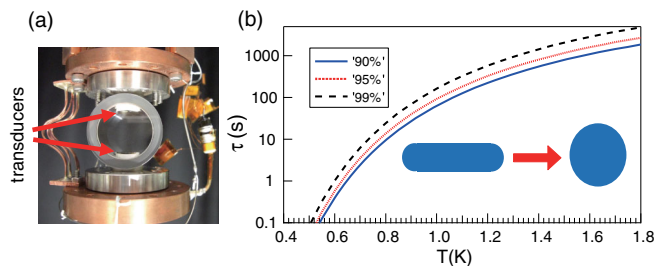


FIG. 2. (a) Photograph of the high-pressure sample cell designed for the zero-gravity experiments in the jet plane. The cell had circular sapphire windows for visualizing the $^4$He crystals in superfluid. Ultrasound transducers to manipulate the crystals were installed in the upper and lower positions of the cell. (b) Relaxation time of a thin circular $^4$He crystal to a sphere with radius of $R_{eq} = 9$ mm as a function of temperature. The lines represent the time required to reach 90%, 95%, and 99% of $R_{eq}$. Adapted from Takahashi, Nomura, and Okuda, 2012b.

with liquid $^4$He through a flow impedance from the $^4$He bath. An ordinary dilution refrigerator was used with a tube-in-tube heat exchanger. The cryostat was 400 mm in diameter, 890 mm in height, and 80 kg in weight. Oil-free scroll pumps were used for the pumping of the 1-K pot and for circulating the $^3$He. Although no special care was taken for the reduced gravity operation other than the use of oil-free scroll pumps, a minimum temperature of about 120 mK was maintained for 20 s under zero gravity.

The cryostat had optical windows aligned in a straight line for visual observation of the $^4$He crystals. Infrared filters were installed between the windows on 70- and 4-K thermal shields. $^4$He crystals were grown in a high-pressure sample cell, thermally anchored to the mixing chamber of the refrigerator. The $^4$He crystals were illuminated through the backside widow by a parallel light [shadow graph method (Settles, 2001)] and observed from the front window using a high-resolution charge-coupled device camera. Figure 2(a) shows a photograph of the sample cell. The cell body was made of stainless steel and the top and bottom flanges were made of oxygen-free–high-conductivity copper. Sapphire plates were metallized and hard soldered on both end sections of the cylindrical part of the sample cell as windows for observations (Okuda and Nomura, 2008). The windows allowed a wide circular visible region. The windows were 24 mm in diameter and the distance between the two windows was 20 mm. Ultrasound transducers were placed in the upper and lower parts of the sample cell to manipulate the crystals by acoustic radiation pressure, as shown in Fig. 2(a) (Nomura *et al.*, 2003, 2004; Abe *et al.*, 2006). Observations were made at the equilibrium crystallization pressure $P_0$, where the superfluid liquid and the crystal coexisted. Thanks to the high crystallization rate, the pressure of the system was uniform and stayed at $P_0$ without any pressure control.

Initially, a $^4$He crystal larger than $l_c$ was placed on the bottom of the sample cell. The crystal exhibited a horizontal plane owing to the gravity. This can be regarded as the equilibrium shape that minimizes the sum of the gravitational energy and surface free energy. When the gravity was reduced to zero, the crystal shape was no longer in the minimum

energy state but in an out-of-equilibrium state and would relax to the ECS determined solely by the surface free energy. This is the process examined in this section.

### B. Relaxation time

We consider why the ultralow temperature environment is necessary to observe the relaxation to the equilibrium shape of $^4$He crystals. The relaxation time $\tau$ of the crystal shape can be estimated using a simplified isotropic model, in which $\alpha$ and $K(T)$ are isotropic, as presented by Takahashi, Nomura, and Okuda (2012b). Suppose that initially the crystal shape on a plate is a circular disk under gravity with a curved side surface, as illustrated in the inset of Fig. 2(b). The curvature radius of the side surface $R_0$ is of the order of $l_c \approx 1$ mm. After the sudden disappearance of gravity, the crystal relaxes to an equilibrium spherical shape with a radius $R_{eq}$ to minimize the surface free energy, which is the driving force for the relaxation.

Taking $R(t)$ as the curvature radius of the crystal at time $t$, the equation of motion of $R(t)$ is given as

$$\dot{R}(t) = -K(T)\Delta\mu, \tag{5}$$

where

$$\Delta\mu = -\frac{1}{\rho_C}\left\{\alpha\left(\frac{2}{R}\right) + \lambda\right\} \tag{6}$$

is the driving force for the transformation of the crystal. We introduce a parameter $\lambda$, which should be determined by the restriction that the total volume of the crystal is constant during the relaxation. In the final state where $R = R_{eq}$, $\Delta\mu$ should vanish. Then $\lambda$ is determined by

$$\lambda = -\frac{2\alpha}{R_{eq}}. \tag{7}$$

By integrating Eq. (5), $t$ and $R(t)$ are related as

$$t = \left(\frac{\rho_C}{2\alpha K(T)}\right)\left\{R_{eq}^2 \ln\left(\frac{R_{eq} - R_0}{R_{eq} - R(t)}\right) - R_{eq}[R(t) - R_0]\right\}. \tag{8}$$

Using the reported $K(T)$ for the rough surface (Bodensohn, Nicolai, and Leiderer, 1986), $\tau$ at which $R(t)$ reaches 90%, 95%, and 99% of $R_{eq}$ can be calculated from Eq. (8) as presented in Fig. 2(b). Here $R_{eq} = 9$ mm was used. The relaxation time is highly temperature dependent, reflecting the temperature dependence of $K(T)$. At high temperatures, for example, at 1.6 K, more than $10^3$ s is required to reach equilibrium. Indeed, at 1.6 K no response of a $^4$He crystal was observed in zero gravity in 20 s. Below 0.6 K, however, $\tau$ is less than 1 s and the relaxation should be completed during the parabolic flight.

### C. Relaxation to equilibrium crystal shape

In this section, the apparent flat surfaces are simply called facets. In Sec. III.D, however, it is shown that they are vicinal surfaces with a small inclination and that the true facets exist only in a small portion at the center. To be more precise, they should be called facetlike flat surfaces.
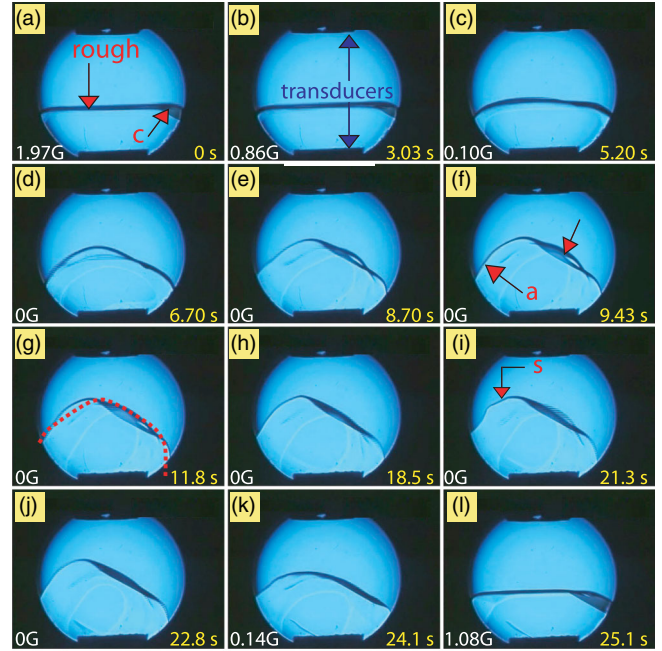


FIG. 3. Change of the $^4$He crystal shape when gravity was reduced to zero. Under gravity, a rough horizontal surface covered most part of the crystal, with a $c$ facet appearing in a small portion of the crystal in the vicinity of the right-hand wall, as indicated by the arrows in (a). The gravity value and time elapsed are indicated in each frame. As the gravity was reduced, the crystal changed its shape as shown in (c)–(e) and relaxed to the different stable shapes (f)–(j) under zero gravity, while flat surfaces correponding to $c$, $a$, and $s$ facets appeared. After the gravity was recovered [(k) and (l)], the crystal retraced the same change and relaxed back to the initial shape. From Takahashi *et al.*, 2015.

Relaxation of a $^4$He crystal with a $c$ facet at a nonhorizontal position is shown in Fig. 3 (Takahashi *et al.*, 2015). The experiment was performed at 150 mK. The elapsed time and gravity value are presented in each frame. Initially, the crystal was under gravity [Fig. 3(a)] and a rough surface was dominant and horizontal, minimizing the gravitational energy. A small $c$ facet was evident near the right-side wall, as indicated by the arrow. As the gravity began to decrease [Fig. 3(b)], a rough surface grew toward the upper-left direction, resulting in expansion of the facet [Figs. 3(c)–3(f)]. An $a$ facet appeared on the left side of the crystal [Fig. 3(f)] and an $s$ facet emerged between the $c$ and $a$ facets [Figs. 3(f)–3(j)], although it was often blurred by vibrations caused by air turbulence. This was the first direct recognition of an $s$ facet in an equilibrium state. An $s$ facet was previously observed on a slowly growing $^4$He crystal below 365 mK (Wolf, Balibar, and Gallet, 1983) and was reported to have an angle of 58.5° to the $c$ facet (Balibar, Alles, and Parshin, 2005). This was consistent with our observation. Even under zero gravity, the crystal never spontaneously detached from the sample cell wall or floated in the superfluid. This was due to the relatively strong partial wetting of the crystal to the wall; the contact angle was approximately 135° (Sasaki, Caupin, and Balibar, 2008). As soon as the gravity was recovered after 20 s of zero gravity, the crystal regained the initial shape [Figs. 3(k)–3(l)] through a reverse
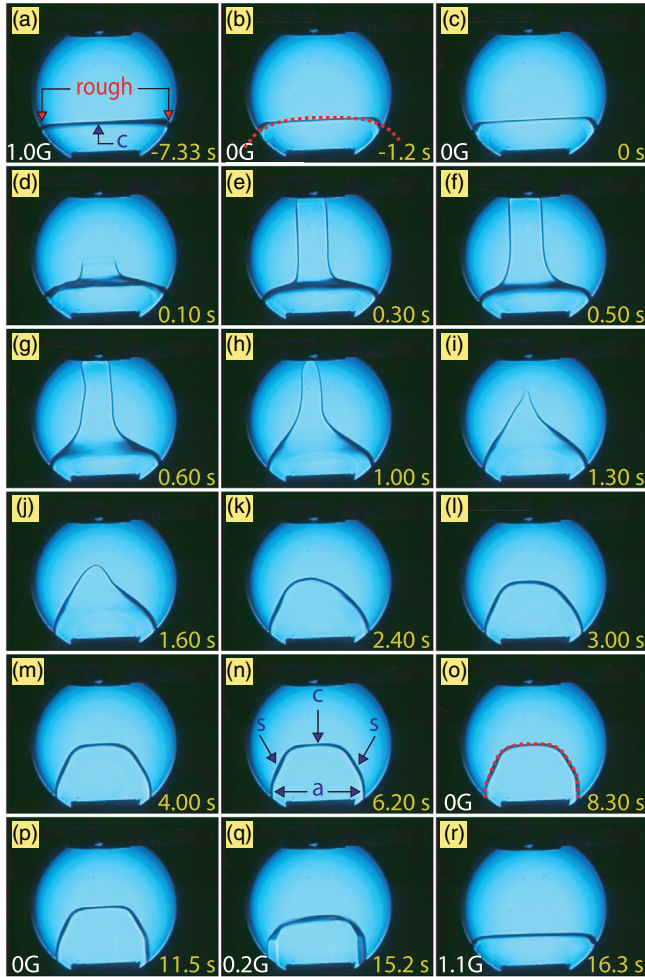
FIG. 4. Change of the $^4$He crystal shape when gravity was reduced to zero. In this case, a nearly horizontal $c$ facet covered most of the crystal and a rough surface appeared in a small portion of the crystal in the vicinity of the wall under gravity, as indicated by the arrows in (a). The gravity value and time elapsed are indicated in each frame. The reduction of gravity did not significantly affect the crystal shape, as shown in (b) and (c). (d)–(f) Deformation process of the $^4$He crystal by an acoustic radiation pressure pulse. (g)–(p) Subsequent relaxation process after the pulse was turned off. Flat surfaces corresponding to $c$, $a$, and $s$ facets appeared. After the gravity was recovered [(q) and (r)], the crystal relaxed back to the initial shape of (a). From Takahashi *et al.*, 2015.

process. A video clip of Fig. 3 is provided in the Supplemental Material (161) as movieFig3.

The relaxation of a $^4$He crystal with a $c$ facet at an almost horizontal position is shown in Fig. 4 (Takahashi *et al.*, 2015). It was found that the crystalline orientation with respect to gravity strongly influenced the relaxation process. The process in Fig. 4 was completely different from that in Fig. 3. In Fig. 4(a), under gravity a large $c$ facet covered most of the crystal surface. No rough surface appeared except for a small region near the contact point with the wall, as indicated by the arrows. While the gravity was reduced, no significant interface motion of the crystal was observed initially, as shown in Figs. 4(a)–4(c). The only noticeable change was that the contact point with the wall slightly lowered due to melting and

the curvature of the rough surface in the vicinity of the wall decreased, reflecting the divergence of $l_c$ [Fig. 4(c)]. Since the crystal changed its shape at a constant volume, any melting is necessarily accompanied by a growth in other parts. A closer inspection shows that the $c$ facet moved slightly (by about 160 $\mu$m) in the vertical direction (Takahashi, Nomura, and Okuda, 2016), but this small motion is barely identified at the scale of Fig. 4.

The crystal as a whole, not only the rough surface near the wall but also the $c$ facet away from the wall, responded to the reduction of gravity. Although the response was small, the shape observed in zero gravity might be regarded as the equilibrium shape under the given boundary conditions imposed by the cylindrical cell wall. However, the $c$ facet covered most of the crystal surface and there were no $a$ facets. The observed shape in Fig. 4(c) was presumably a metastable shape set by the wall.

To investigate whether the crystal, which was covered dominantly with the horizontal $c$ facet, is really metastable and can escape from this shape by a large perturbation, an acoustic wave pulse was applied from the lower part of the cell. The acoustic wave of 10 MHz hit the interface in the upward direction for 0.5 s. It was found that acoustic radiation pressure induces crystallization, which is explained in Sec. VII in detail. The central region of the $c$ facet was cylindrically deformed or crystallized by the acoustic radiation pressure, moving upward and reaching the ceiling [Figs. 4(d)–4(f)]. After the acoustic wave pulse was turned off, the top of the cylinder detached from the ceiling and became rounded [Fig. 4(h)], then changed into a conelike shape [Fig. 4(i)] that was absorbed into the main body of the crystal [Figs. 4(j)–4(l)]. While the crystal shape in Fig. 4(k) was rounded and the $c$ facet completely disappeared from the interface due to the large perturbation, $c$, $a$, and $s$ facets subsequently appeared from the rounded shape [Fig. 4(m)]. Thus, the deformation by the acoustic wave pulse allowed the crystal to escape from the metastable state, and the shapes shown in Figs. 4(m)–4(o) are considered to be the ECSs. When the gravity returned [Figs. 4(q) and 4(r)], the crystal recovered the initial shape as in Fig. 4(a). A video clip of Fig. 4 is provided in the Supplemental Material (161) as movieFig4.

Although the relaxed shapes in Figs. 3(f)–3(j), Figs. 4(b) and 4(c), and Figs. 4(m) and 4(o) look different at first sight, the red dotted curves in Figs. 3(g), 4(b), and 4(o) are homothetic. Therefore, they actually had similar shapes but were cut in different ways by the cell wall. Additionally, the similar shape was realized through completely different relaxation processes; the left-hand side of the $c$ facet grew while the right-hand side melted in Fig. 3, the rough surface near the wall melted, and the $c$ facet grew a little vertically in Figs. 4(b) and 4(c), and the $c$ facet appeared with melting after the large deformation in Figs. 4(h)–4(o). These support the assumption that each crystal reached at least near the equilibrium state under the given boundary condition and justify the following analysis.

**D. Analysis of equilibrium crystal shape**

Once a crystal reaches equilibrium, we can analyze the shape using the established theory for the ECS (Takahashi *et al.*, 2015). Wulff developed a graphical method, known as

the Wulff construction, to determine the ECS from the orientation dependent surface free energy and derived several basic properties of the ECS. The Wulff theorem (Wulff, 1901) guarantees the following relation for any *i*th plane of the crystal surface when a crystal is in the equilibrium state:

$$\frac{\alpha_i}{h_i} = \frac{\rho_C \Delta\mu}{2}, \tag{9}$$

where $\alpha_i$ is the interfacial free energy of the *i*th plane and $h_i$ is the distance between the *i*th plane and the origin of the polar plot in the Wulff construction (Wulff's origin) of the ECS. Although $\Delta\mu = 0$ for an infinitely large crystal, $\Delta\mu \neq 0$ for a finite size crystal, though an accurate value cannot usually be determined easily.

Since the ECS was obtained in Fig. 4, Wulff's origin can be determined, allowing us to analyze the crystal shape in detail. Suppose that the perpendicular bisectors of the *c* and *s* facets pass through the origin, neglecting a small orientation dependence of the interfacial free energy around an *s* facet. Since the *s* facets appeared clearly, the position of the origin could be specified with a reasonably good accuracy and is indicated by the open circle in Fig. 5 for the relaxed crystal shape of Fig. 4. The dashed lines in Fig. 5 are the perpendicular bisectors of each facet. Once the origin is determined, the distances between the origin and each facet $h_i$ can be measured from the images. $\Delta\mu$ and the interfacial free energies of the *a* and *s* facets $\alpha_a$ and $\alpha_s$ were determined from Eq. (9), relative to the known value of the *c* facet $\alpha_c = 0.172$ erg/cm$^2$ (Andreeva and Keshishev, 1991).

The radius of the *c* facet $R_F$ is expressed as $\beta/a\rho_c\Delta\mu$ and is successfully determined from Eq. (9) as

$$R_F = \frac{\beta h_c}{2a\alpha_c}, \tag{10}$$

where the indices represent the values of the *c* facet and *a* is the step height on the facet. As for the *c* facet of the $^4$He crystal, the ratio between the step free energy [$\beta/a \sim 0.014$ erg/cm$^2$ (Rolley *et al.*, 1995)] and the surface free energy $\beta/a\alpha_c$ can be determined to be approximately 1/10 due to the large

quantum fluctuation of the steps. $R_F$ should be much smaller than the crystal size (or $h_c$) and was found to be represented by the region between the two open arrows in the enlarged figure, Fig. 5(a). The true facet size should be much smaller for the *a* and *s* facets. The region indicated by the arrows may not correspond with the size of the apparent *c*-facet surface. This discrepancy was resolved by considering the vicinal surface shape as follows.

An equilibrium crystal profile of a *c* facet and the adjacent vicinal surface was theoretically predicted, as shown in Eq. (11), assuming a repulsive step-step interaction energy of the form $\sigma/r^2$ (Marchenko and Parshin, 1980; Jayaprakash, Saam, and Teitel, 1983; Akutsu, Akutsu, and Yamamoto, 1988; Uwaha and Nozières, 1989):

$$z(x) = -\frac{2}{3}\sqrt{\frac{a^3\rho_c\Delta\mu}{3\sigma}}(x - R_F)^{3/2}, \tag{11}$$

where *z* represents the height variation from the facet ($z = 0$), *x* ($x \geq R_F$) denotes the distance from the center of the facet, $\sigma$ is the step-step interaction coefficient, and *r* is the step interval. It is known that the dominant interaction energy has both elastic and entropic origins (Rolley *et al.*, 1995). Using the obtained $\Delta\mu$ and the known step-step interaction coefficient $\sigma/a^3 \sim 1.63$ erg/cm$^2$ (Keshishev and Shemyatikhin, 2008), the vicinal surface profile of Eq. (11) forms a solid curve along the crystal surface, as in Fig. 5. The theoretical curve is consistent with the observed crystal shape, which appears as the thick line in this scale. The vicinal surface does incline but the inclination is so small near the facet that it appears to be nearly flat around the *c*-facet edge at the resolution of the crystal image. This is why the apparent *c*-facet surface looked much wider than $2R_F$. $z(x)$ deviates from the crystal surface in the region indicated by the two-headed arrow in Fig. 5(a), where the vicinal surface is not well described by the step model and crosses over to an isotropic rough surface (Rolley *et al.*, 1994, 1995).

Babkin *et al.* (1995) reported an anomalous surface state in the vicinal region close to the *c* facet using a high-resolution interferometer. The observed side view of the crystal shape in Fig. 5 did not have enough resolution to compare with their result.

## IV. ULTRAFAST OSTWALD RIPENING OF $^4$He CRYSTALS UNDER ZERO GRAVITY

When a large number of crystals coexist in a saturated aqueous solution, the size distribution of the crystals changes over time. Ostwald ripening is a process in which smaller crystals melt and larger ones grow to minimize the overall surface energy, which is proportional to the total surface area (Ostwald, 1900; Lifshitz and Slyozov, 1961). It occurs in many systems, from bubbles to melting crystals. A familiar example is old ice cream becoming gritty. In ordinary classical materials, the process is extremely slow. Typically it takes many months, and the largest crystal is at most at micrometer scale. $^4$He quantum crystals, however, are an exceptional material for which the ripening process proceeds via a swift superflow. In particular, in a zero-gravity environment we can observe Ostwald ripening of extremely large $^4$He crystals,
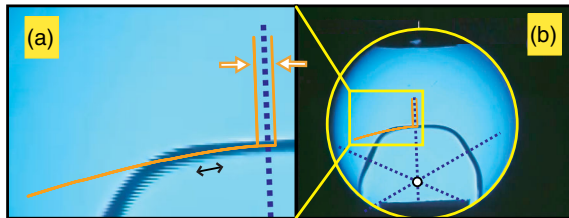


FIG. 5. Magnified views of Fig. 4(o) under zero gravity. The rectangular region in (b) is expanded in (a). The orange solid line shows the theoretical shape of the vicinal surface given by Eq. (11) compared with the crystal surface. The narrow area between the open arrows is the true *c* facet of the diameter, $2R_F$ given by Eq. (10). Around the two-headed arrows, the curve deviates from the surface. The open circle in (b) is the intersection between the perpendicular bisectors (dashed lines) of the *c* and *s* facets, indicating the origin in the Wulff construction. From Takahashi *et al.*, 2015.
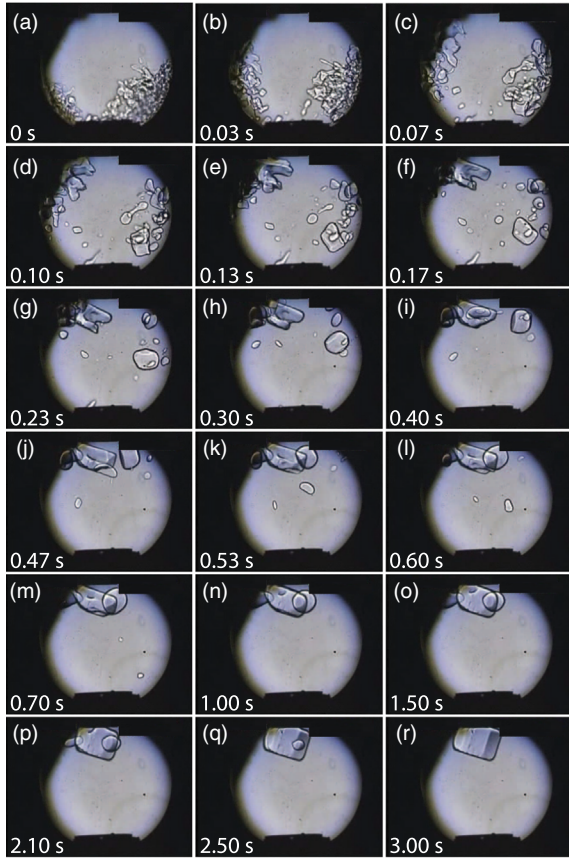
FIG. 6. Temporal evolution of splashed ⁴He crystals by an acoustic wave pulse under zero gravity. The time is indicated in each frame. The temperature was 0.67 K and the pulse was applied from a transducer, seen in the lower part, at 0 s. (a) Initially there were tens of small crystals. (r) Ostwald ripening occurred and continued until only the largest crystal survived at 3.0 s. From Takahashi *et al.*, 2012.



FIG. 7. Temporal evolution of the sizes of several selected crystals in Fig. 6. From Takahashi *et al.*, 2012.

governed by the surface energy without limitation of the capillary length.

Ostwald ripening of ⁴He crystals in superfluid has been observed after crushing by acoustic waves under zero gravity (Takahashi *et al.*, 2012). The temporal evolution of the crushed ⁴He crystals is shown in Fig. 6. The temperature was initially 0.67 K and was heated to 0.75 K by the acoustic wave pulse in about 3 s. At 0.03 s, many small crystals with irregular shapes were formed, and at 0.10 s more than ten crystals of different sizes could be recognized. Smaller crystals melted and disappeared; three large crystals were present at 1.0 s, and eventually only the largest one survived. At 1.0 s the largest crystal was facetted with $c$ and $a$ facets, while the others were rounded and covered with a rough surface. It is generally known that facets expand in growing crystals and rough surfaces expand in melting crystals, as illustrated in Figs. 1(c) and 1(d). The largest surviving crystal was about 6.5 mm. It was also observed that the ripening did not finish in 20 s for a larger amount of the crystals. A video clip of Fig. 6 is provided in the Supplemental Material (161) as movieFig6.

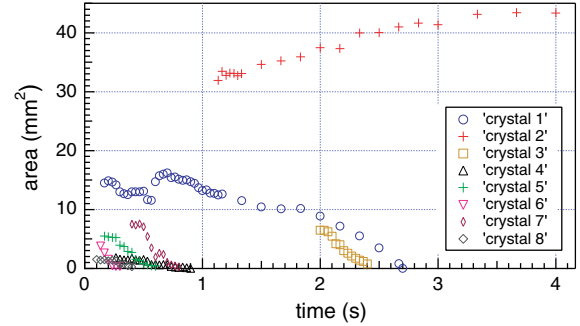A projected area of selected crystals, which has a well-defined shape in Fig. 6, is plotted in Fig. 7 as a function of time. Not all of the crystals were measured because some crystals had an ill-defined shape and some overlapped, preventing an accurate measurement. Although the number of obtained data points is limited, smaller crystals tended to disappear earlier than larger ones, and thus Ostwald ripening is clearly seen.

A similar experiment was performed under gravity on the ground as a comparison. In contrast to the zero-gravity case, it was found that the crystals in the upper region of the cell became smaller and eventually disappeared, while the crystals in the lower region became larger, showing that the crystals under gravity tended to grow to gain gravitational energy at lower positions and did not follow the Ostwald ripening process.

We now consider the ripening process in a superfluid from a slightly different viewpoint. Suppose that $P_0$ is the equilibrium pressure of an infinitely large flat superfluid-crystal interface. For a finite size crystal with an interface curvature radius of $R$, the equilibrium liquid pressure increases as

$$P_L(R) = P_0 + \frac{2\rho_L \alpha}{\Delta \rho R}. \qquad (12)$$

Therefore, the liquid pressure around the small crystals is higher than that of the larger crystals. A superfluid "knows" the spatial pressure landscape and flows swiftly to decrease the total energy.

On the other hand, Ostwald ripening of ordinary classical materials proceeds via a diffusion of atoms or heat, which is a random walk process to lower the energy. If it takes 1 month to grow crystals up to micrometer size and if the time for the diffusion is scaled by the square of the length, it should take $10^6$ months to complete the ripening at millimeter scale. But for ⁴He, the ripening finished in a few seconds, accelerated by the superfluidity of the quantum liquid. It would be revealing to compare theoretically the size distribution in the coarsening dynamics for the classical diffusion case and the superflow case (Hofmann, Natu, and Das Sarma, 2014; Williamson and Blakie, 2016; Fujimoto, Hamazaki, and Ueda, 2018; Takeuchi, 2018). It would also be interesting to know the effect of faceting, which causes much slower crystal growth than melting, on the size distribution compared with that of isotropic fluids such as phase separated superfluids.

Finally, it should be noted that Eq. (12) was recently confirmed by a direct measurement showing the finite size effect of a ⁴He crystal (Todoshchenko, 2018).

# V. FALLING $^4$He CRYSTALS IN SUPERFLUID

First-order phase transitions under heat or mass flow in statistical physics can be used to explore possible general descriptions of nonequilibrium systems (Oono and Paniconi, 1998; Sasa and Tasaki, 2006; Onuki, 2007; Teshigawara and Onuki, 2008). The extremely high crystal growth rate of $^4$He at low temperatures is thought to make crystal shapes sensitive to the heat flow or superflow around the crystals, thus opening the possibility that the effect of these flows on the first-order phase transition can be visualized via a crystal shape change. Indeed, Kapitza resistance and the Onsager cross coefficient have been determined by taking the $^4$He crystal deformations into account under heat flow (Wolf, Edwards, and Balibar, 1983). Kapitza resistance defines the temperature jump at the interface under the heat flow, and the Onsager cross coefficient is the ratio between the crystal growth velocity and the heat flow. However, few experimental trials have investigated the effect of superflow on $^4$He crystals (Maksimov and Tsymbalenko, 2002; Tsymbalenko, 2013, 2015), since it is not easy to induce a uniform and steady superflow experimentally. This difficulty can be overcome by utilizing falling $^4$He crystals in superfluid and visualizing their motion with a high-speed camera. The crystals are subjected to a fairly uniform superflow from beneath, transforming their shape quickly and drastically during the falling.

The following sections describe experiments conducted under gravity on the ground.

## A. Simple falling

An experiment was performed on the ground in a conventional $^3$He-$^4$He dilution refrigerator with optical access (Okuda and Nomura, 2008). Superfluid $^4$He was supplied through a capillary to a sample cell up to a few millibars above $P_0$. If the pressurization proceeds slowly enough, a metastable superfluid can exist without forming crystals. An ultrasound pulse was emitted from a transducer installed in the upper part of the cell to initiate nucleation of crystals at 0.3 K (Abe *et al.*, 2005). Right after the pulse, a $^4$He crystal was nucleated on the transducer surface. Superfluid $^4$He was continuously supplied to the cell to grow the $^4$He seed crystal to an appropriate size on the transducer. We then stopped the supply. The crystal shape was a hexagonal prism whose upper part was cut by the transducer obliquely, as shown in Fig. 8(a). As it grew too large to remain attached to the transducer, it eventually fell into the superfluid, as shown in Figs. 8(b)–8(o), and came to rest as shown in Figs. 8(p)–8(r) (Nomura *et al.*, 2014). The distance between the transducer and the bottom was 10 mm. A video clip of Fig. 8 is provided in the Supplemental Material (161) as movieFig8.

While the crystal was falling in the superfluid, its rounded corners between the adjacent facets became sharper on the lower surface; the facets expanded and the rough surface between them shrank, as seen in Fig. 8. At the same time, its upper surface became horizontal with a small undulation. This upper surface was actually a rough surface. While the $^4$He crystal was moving it was subjected to an upward superflow, causing the drastic transformation. The lower surface faced
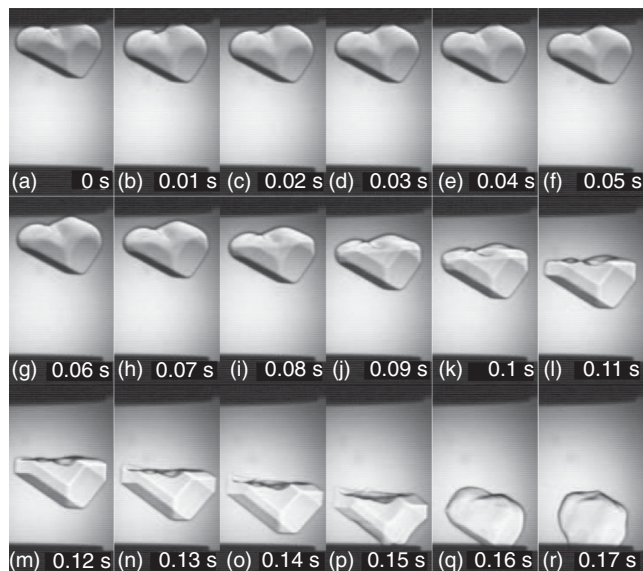


FIG. 8. A falling $^4$He crystal in superfluid. The time is indicated in each frame. The temperature was 0.3 K. The crystal (a) detached from the transducer surface, (b)–(o) fell in the superfluid liquid, changing shape, and (p)–(r) came to rest at the bottom. From Nomura *et al.*, 2014.

the incoming superflow, which induced the crystal growth, while the upper surface experienced the outgoing superflow, which induced the melting. Generally, an expansion of facets is observed in the growth shape, whereas an expansion of rough surfaces is observed in the melting shape, as illustrated in Figs. 1(c) and 1(d). An interesting point regarding the falling crystal is that both growth and melting shapes appeared at the same time in different parts of the crystal subjected to the unidirectional upward superflow. The facets were so stable that no sign of Kelvin-Helmholtz instability was found even under this superflow on the lower surface. The small undulation on the upper surface can be caused by crystal defects such as grain boundaries (Sasaki, Caupin, and Balibar, 2008) or by Kelvin-Helmholtz instability, but the origin has not yet been clarified.

When the crystal reached the bottom, it no longer faced the superflow and changed its shape quickly, adjusting to the new boundary condition set by the wall, as shown in Figs. 8(p)–8(r). The contact angle between a $^4$He crystal in superfluid and a solid wall is known to be about 135° (Sasaki, Caupin, and Balibar, 2008). Thus, the wettability on the wall drove the deformation. In Fig. 9, magnified images of the crystal in the vicinity of the impact position are shown for a period of 1 ms. It is seen that a pulselike deformation wave propagates on the crystal, as indicated by the arrows. The propagating velocity was estimated to be about 70 cm/s.

Such a quick crystal shape change did not occur in the collision with the sample cell base at high temperatures, indicating that the observed crystal shape change was not induced by the plastic deformation inside of the crystal, but by the crystallization and melting on the surface. The pulselike deformation wave must be a crystallization wave. Thus, the collision shown in Fig. 9 is in a peculiar limiting case in that the
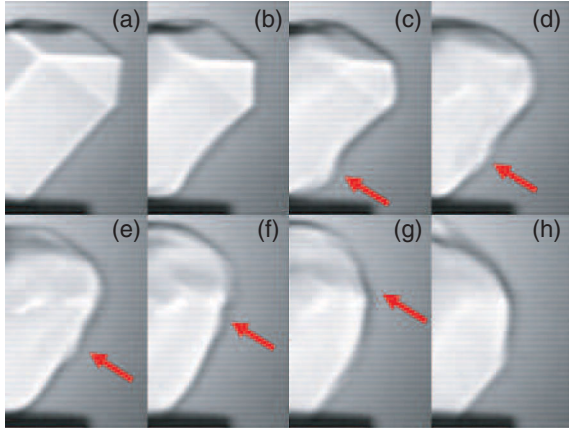
FIG. 9. Magnified images of the crystal when it collided with the bottom in Fig. 8. The images are shown for every 1 ms. A pulselike crystallization wave was generated at the impact point and traveled around the surface as indicated by the arrows. From Nomura *et al.*, 2014.

first-order phase transition took place quickly coupled closely to the superflow. Collisions between objects are common phenomena and are important in diverse fields. While elastic or plastic processes are usually dominant for classical objects, they are not so for ⁴He crystals with an extremely high crystallization rate. For ⁴He crystals the effects of elasticity and plasticity are negligible compared to the rapid phase transition that governed the collision dynamics of the quantum crystal.

The position of the lowest point of the crystal $y$ was measured as a function of time $t$ and plotted against $t^2$ in Fig. 10. A linear dependence was found in the early stage of roughly $t < 0.1$ s, indicating that the crystal experienced a constant acceleration motion. The solid line is a linear fitting curve in the early stage. The acceleration was obtained to be $a = (0.059 \pm 0.003)g$.

For an object of mass $m$, volume $V$, and density $\rho_C = m/V$ falling in a viscosity-free and incompressible fluid of density $\rho_L$, the effective force is reduced by the buoyancy as $f = \Delta \rho m g / \rho_C$. The effective mass is enhanced to $m + m'$ by the surrounding liquid flow. In the case of a spherical object, $m' = \rho_l V/2$ (Landau and Lifshitz, 1987), and thus
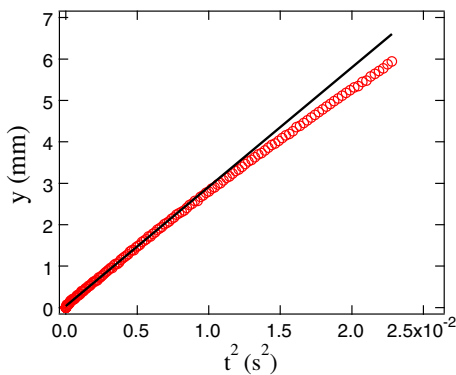


FIG. 10. Position of the lowest part of the falling ⁴He crystal shown in Fig. 8 plotted against $t^2$. The solid line is a linear fitting at the early stage of falling, showing a constant acceleration motion during that period. From Nomura *et al.*, 2014.

$m + m' = m(1 + \rho_L/2\rho_C)$. Therefore, the acceleration of the spherical object can be obtained as

$$ a = \frac{\Delta \rho g}{\rho_C + \rho_L/2}. \tag{13} $$

Using the physical parameters of ⁴He (Wilks, 1967), we obtain $a = 0.069g$. This value is roughly consistent with the observed acceleration of a ⁴He crystal with an accuracy of about 15%. The actual crystal shape was not spherical and a better estimation of the effective mass for the observed crystal shape would improve the agreement.

The agreement with this simple estimation means that the crystallization and melting had a minimal effect on the falling process, since the lower surface was primarily covered by facets with slow growth. This is in clear contrast to the rising of a superfluid droplet in a crystal discussed in Sec. VI, in which crystallization and melting sorely determined the rising process.

In the later stage, the acceleration deviated from a linear dependence because dissipation set in. It deviated at around $t \approx 0.1$ s, where the falling velocity reached about 6 cm/s. The origin of the dissipation is likely to be the formation and/or expansion of quantized vortices in the superfluid liquid.

Tsymbalenko reported a pressure variation during the falling of a ⁴He crystal measured by a high-speed pressure sensor. The crystal investigated was not covered by slow facets but by a highly mobile surface. He was able to explain the pressure variation by taking the interface dynamics into account (Tsymbalenko, 2019).

### B. Falling when touching a needle

Although the crystal shape was modified by the superflow for simple falling, the falling was estimated to be nearly constant acceleration motion. What would happen if an obstacle was placed on the falling path of the crystal? We found that the falling behavior was drastically changed when a tungsten needle of 100 $\mu$m diameter with a sharpened tip was placed close to the path of the crystal. The needle position was such that the crystal edge just hit the tip, as shown in Fig. 11 (Nomura *et al.*, 2014).

In this experiment, the ⁴He crystal fell with its $c$ facet nearly horizontal, at 0.4 K. The lower and side surfaces were completely faceted and stable, while the upper surface was rough, as in the simple falling case. When the crystal came close to the needle, its edge extended slightly to be hooked by the needle, as shown in Figs. 11(b)–11(d). The crystal rotated slightly around the needle during the contact and stopped the rotation immediately after detaching from the needle. Thereafter, the facet on the side surface became a rough surface and showed a fluttering motion. This fluttering motion, seen in Figs. 11(e)–11(q), is likely to be a crystallization wave or a kind of Kelvin-Helmholtz instability agitated by the surrounding superflow. The fluttering motion occurred as soon as the facets disappeared, showing that the facets were more stable against instability than the rough surfaces. Kelvin-Helmholtz instability (Uwaha and Nozières, 1986) is again discussed in Sec. VIII. Stopping rotation is nontrivial in a superfluid, probably because of dissipation by the fluttering motions. Finally,
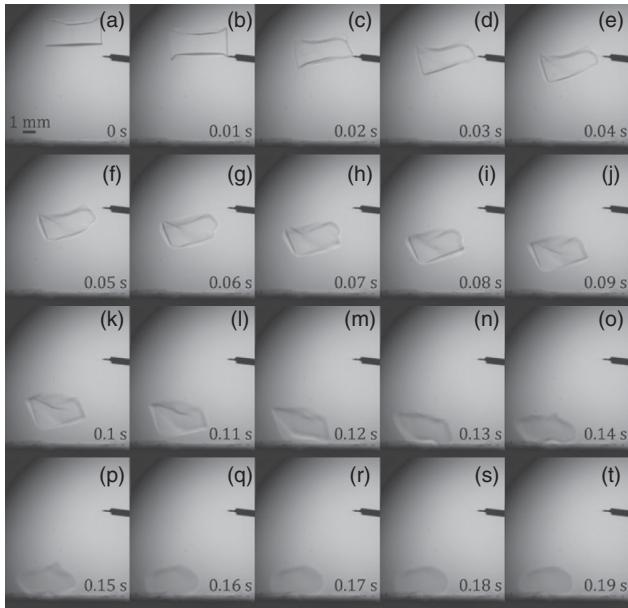
FIG. 11. Falling of a ⁴He crystal in superfluid disturbed by a needle. The time is indicated in each frame. The temperature was 0.4 K. The crystal (b)–(d) was slightly tilted when hooked by the needle and (e)–(q) fell while exhibiting drastic deformation. (r)–(t) It finally came to rest on the bottom. From Nomura *et al.*, 2014.

the crystal settled on the bottom, as shown in Figs. 11(r)–11(t). A video clip of Fig. 11 is provided in the Supplemental Material (161) as movieFig11.
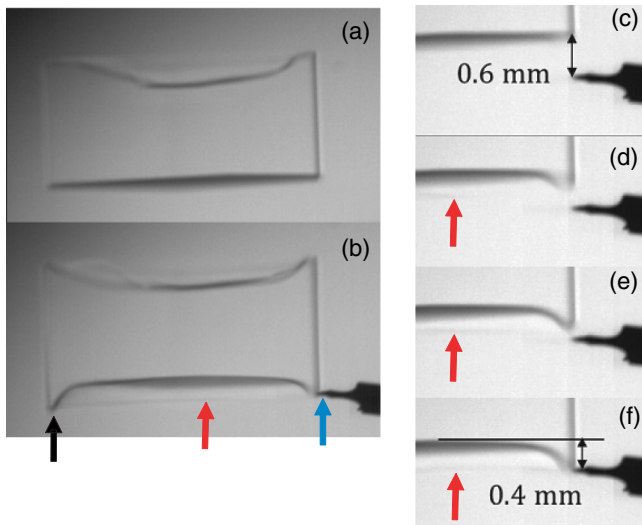


FIG. 12. Magnified images of a falling ⁴He crystal before and at contact with the needle in Fig. 11. The overall shapes of the crystal before and at the contact point are shown in (a) and (b). Images around the needle are shown in (c)–(f) at every 1 ms. Before the contact, the rim of the *c* facet was attracted to the needle. The deformation was unexpectedly large and anomalously extended to the other side of the facet edge. The blue (right), black (left), and red (middle) arrows in (b) show the needle, the protrusion of the edge at the other side, and the protruding rim, respectively. From Nomura *et al.*, 2014.

The crystal shape before contact with the needle is shown in Fig. 12(a), and its deformation at the instant of contact is shown in Fig. 12(b). Magnified images around the needle are shown in Figs. 12(c)–12(f) for every 1 ms. Even before the horizontal *c* facet reached the needle, the *c*-facet edge protruded toward the needle, indicating the existence of a long-range attractive interaction between the surface of the falling crystal and the needle. The other side of the facet, far from the needle, protruded almost simultaneously with the close edge. The crystal was deformed as a whole and the rim around the *c* facet protruded at the moment of contact. In Fig. 12, the blue arrow indicates the needle and the black arrow indicates the protrusion of the other side. The thin line parallel to the *c* facet indicated by the red arrows shows the protruded rim. The rim protruded at a velocity of about 15 cm/s, which was significantly faster than the falling velocity of 5 cm/s.

Before the contact, the ⁴He crystal shape was stationary and thus the surrounding superflow was tangential to the crystal surface in the frame moving with the crystal. When the crystal approached the needle, it disturbed the nearby superflow profile, which is probably the origin of the attractive interaction and the rim-shape deformation. However, details of the superflow profile are not known and the true mechanism of the interaction is not clear at present. A simulation study of the superflow profile taking the crystallization process into account on an equal footing would explain the unexpected behavior of the falling ⁴He crystal.

## VI. RISING SUPERFLUID DROPLETS IN ⁴He CRYSTALS DUE TO BUOYANCY

Liquid or gas inclusions are occasionally formed in a crystal. When inclusions have an anisotropic shape reflecting the anisotropy of the host crystal, they are sometimes called negative crystals (Nelson, Mazey, and Barnes, 1965; Pavlovska and Nenow, 1971). Negative crystals have been used to investigate the ECS because they are free of contaminants and external effects such as those arising from the container wall. Their motion has also been observed. For example, negative crystals in ice can migrate under a small temperature gradient due to evaporation on one side and condensation on the other (Nakaya, 1956). It is natural to ask what negative crystals of ⁴He look like (Polturak *et al.*, 1995; Okuda *et al.*, 1998). Superfluid droplets forming in a ⁴He quantum crystal, which can be referred to as quantum negative crystals, have been investigated in bcc and hcp phases by visualizing their shapes and motions at various temperatures (Yoneyama, Nomura, and Okuda, 2004). They were found to be spherical in the bcc phase and faceted in the hcp phase below 1.3 K. The interface mobility was so high that they steadily rose in the crystal even under a small driving force of gravity, which should be irrelevant for ordinary negative crystals for the short term. Their morphology and motion were found to become anisotropic at lower temperatures due to the roughening transition of the host crystal.

Although it appears to be difficult to form superfluid droplets in a ⁴He crystal, we found several methods to achieve it. Superfluid droplets in bcc ⁴He crystals spontaneously and continuously appeared at the bottom of a sample cell when the bottom was slightly warmer than the top. This appearance can

be viewed as a kind of Rayleigh-Taylor instability (de Gennes, Brochard-Wyart, and Quéré, 2004). It was also possible to nucleate a droplet on an ultrasound transducer acoustically. In this case, the size of the droplet could be adjusted by controlling the power and period of the acoustic wave pulses. Since the density of the negative crystal is different from that of the host crystal, $^4$He atoms have to be extracted for the droplets to form to compensate for the density difference. The mass flow paths can be either through the crystal or through fluidlike layers between the crystal and the wall (or the transducer) (Dash and Wettlaufer, 2005; Mizusaki, Nomura, and Hiroi, 2007), but the actual formation mechanism of the droplets has not yet been confirmed.

When a superfluid droplet formed on the bottom of a cell in the bcc phase at high temperatures above 1.66 K, it rose vertically in the host crystal, as shown in Fig. 13(a). Its shape was spherical, because the crystal surface in the bcc phase is rough. It eventually merged with the bulk superfluid above the host crystal and disappeared. A video clip of Fig. 13(a) is provided in the Supplemental Material (161) as movieFig13a.

It can be concluded that the rising was induced not by the plastic deformation of the host crystal but by the melting and growth of the host, as follows. Steady motion of spherical droplets is realized by melting of the upper surface and crystallization on the lower surface, which moves the center of mass of the droplet upward, as illustrated in Fig. 13(b). The superfluid in the droplet flows in an opposite direction to the droplet motion. Based on this model, the driving force is the gravitational energy or the buoyancy, which is proportional to the height difference of the two surfaces, or the droplet radius $R$ in the case of a spherical droplet. The rising velocity is determined by the interface mobility $K(T)$ and is given in the case of a spherical droplet by (Mukai and Uwaha, 2006)

$$v = K(T)\frac{\Delta\rho}{\rho_C}gR. \tag{14}$$

This size dependence was confirmed by Fig. 4 in Yoneyama, Nomura, and Okuda (2004) and is also shown in Fig. 14. Figure 14 was obtained for a slightly different setup in which the droplet size increased as it rose with slow cooling, as
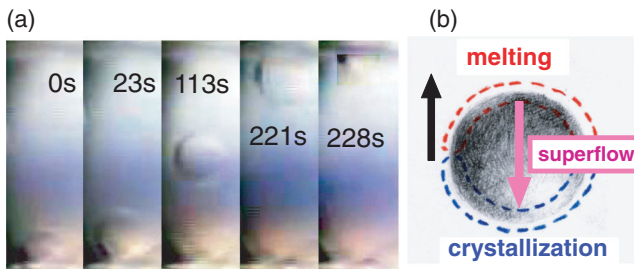


FIG. 14. Rising velocity of superfluid droplets in a bcc $^4$He crystal as a function of the radius. The three symbols represent three different droplets. Since they grew as they rose with slow cooling, $v$ can be obtained as a function of the radius. The upper and lower lines are the calculations of Eq. (14) at 1.49 and 1.63 K. From Takahashi, Nomura, and Okuda, 2012a.

explained at the end of this section. The temperature dependence of the rising velocity was also consistent with this model.

In the hcp phase at temperatures lower than the roughening transition of a $c$ facet $T_{R1}$, the droplet shape became nonspherical. A large $c$ facet appeared in the upper part of the superfluid droplet and a rounded rough surface in the lower part, as shown in Fig. 15. It rose in the crystal, not vertically but obliquely parallel to the $c$ facet. The mobility of the $c$ facet is much lower than that of the rough surface, which is why the crystal moved parallel to the $c$ facet. The droplet shape change is also understandable in consideration of Figs. 1(c) and 1(d). As it rose, the fast-moving rough surface caught up with the slowly moving $c$ facet in the upper part of the droplet. This resulted in a widening of the $c$ facet in the upper part like that in the growth shape. In the lower part, on the other hand, the rough surface led the facet and the facet shrank as in the melting shape. The anisotropic mobility of the interface influenced the morphology of the rising droplets.

The roughening transition temperature of an $a$ facet is about $T_{R2} \approx 1.0$ K. The droplet motions shown in Figs. 15(a) and 15(b) were measured at 0.92 and 0.87 K, respectively. The appearance of an $a$ facet can be seen in Fig. 15(b) as the dark image indicated by the circle. The effect of the $a$ facet can be recognized in the temperature dependence of the rising velocity in Fig. 16. Here droplets with diameters in the range $3.4 \pm 0.3$ mm were chosen. Droplets rose faster at lower temperatures, reflecting the increase of $K(T)$, but slowed down below 0.9 K due to the appearance of $a$ facets. It was demonstrated that the dynamics and morphology of the droplets became successively anisotropic as the temperature lowered. A video clip of Fig. 15(b) and that of rising droplets in a host crystal with a different orientation are provided in the Supplemental Material (161) as movieFig15b and movieFig15_2, respectively.

The detachment of a droplet from the bottom of the cell is also a curious process. Figure 17 shows this detachment process for the bcc phase, showing the droplets stretching and being pinched off. The neck radius $R_n(t)$ was measured as a function of time in the bcc case and found to follow a power

(a)



| 0s | 23s | 113s |
| | 221s | 228s |

(b)

melting

superflow

crystallization

FIG. 13. (a) Pictures of a superfluid droplet in a bcc $^4$He crystal moving vertically upward with an almost spherical shape. The time is indicated in each frame. The temperature was 1.66 K. The diameter of the droplet was 2.8 mm. (b) Schematic of a droplet showing the rising mechanism via melting in the upper part and crystallization in the lower part. The upward and downward arrows show the directions of the center of mass motion and superfluid flow. From Yoneyama, Nomura, and Okuda, 2004.
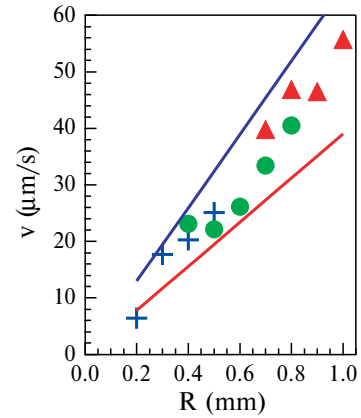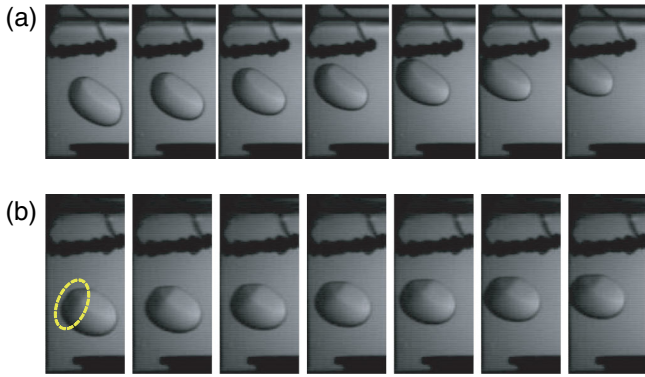
FIG. 15. Superfluid droplets in a hcp ${}^4$He crystal moving upward obliquely parallel to a $c$ facet at (a) 0.92 and (b) 0.87 K. These pictures were taken every 0.24 s. The orientation of the crystal was such that the $c$ facet of the droplet was seen from diagonally above by the camera. The motion in (a) was faster than in (b) because the $a$ facet, indicated by the circle, appeared on the front side of the droplet at the lower temperature. Adapted from Okuda and Nomura, 2008.

law, such that $R_n(t) \propto |-t|^\alpha$ with $\alpha \approx 0.5$ (Okuda and Nomura, 2008). Here $t$ was measured from the moment of pinch-off. Mukai and Uwaha (2006) theoretically analyzed the detachment process with the isotropic interface energy and gravitational energy taken into account. The observed behavior in Fig. 17 was well reproduced by their simulations. They also expected temporal evolution of the neck radius as $R_n(t) \propto \sqrt{|-t|}$ which is consistent with the experimental observation.

A power law behavior was theoretically predicted for the coalescence of two quantum crystals driven by the surface energy, which can be viewed as the inverse process of the pinch-off. The coalescence of two ${}^3$He crystals was examined and the neck radius was shown to follow a power law (Ishiguro *et al.*, 2004), which is consistent with the theory of coalescences (Maris, 2003; Ishiguro *et al.*, 2007).

Finally in this section the observation of spontaneous formation of superfluid droplets in a ${}^4$He crystal on slow cooling is presented (Takahashi, Nomura, and Okuda, 2012a).
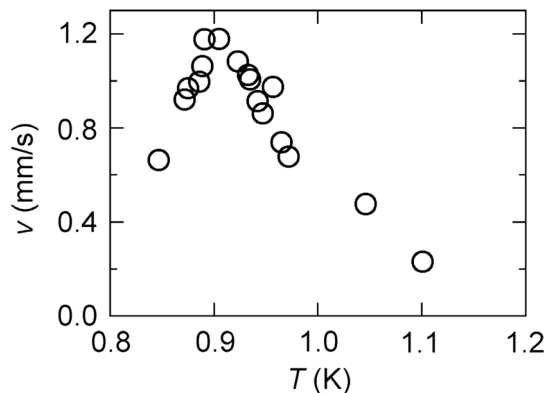


FIG. 16. Temperature dependence of the rising velocity of superfluid droplets in a hcp ${}^4$He crystal. The decrease in $v$ below 0.9 K is a result of the appearance of an $a$ facet on the front side of the droplet, as shown in Fig. 15(b). From Yoneyama, Nomura, and Okuda, 2004.
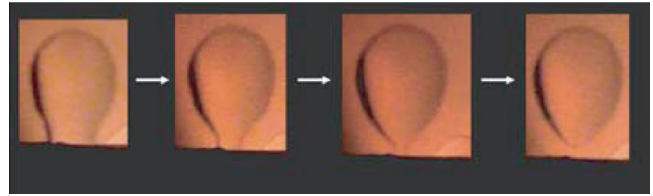


FIG. 17. Superfluid droplet at the instant of detaching from the bottom wall. From Okuda and Nomura, 2008.

Figure 18 shows that numerous small superfluid droplets spontaneously nucleated and grew in the host crystal of the bcc phase. The initial temperature was 1.65 K and the cooling rate was about 1.5 mK/s. Initially, no sign of droplets was recognized in the host. But then several spherical droplets nucleated and grew to about 1 mm in diameter within 20 to 40 s. In the case of formation using temperature gradients or acoustic waves, mentioned earlier, the droplet generation took place on the wall surface. However, in this droplet formation on cooling they appeared inside the ${}^4$He crystal, away from the wall. To compensate for the density difference between the liquid and crystal, a mass flow mechanism inside the crystal is needed. Although the diffusion of the thermally activated vacancies probably carries the mass flow at high temperatures (Birchenko *et al.*, 2018; Nomura, Matsuda, and Okuda, 2018), the formation mechanism of the superfluid droplets is not clear. Nonetheless, it is certain that superfluid droplets can be generated in ${}^4$He crystals by several methods due to mass flow mechanisms in some way inside the quantum crystal or on the wall (Ray and Hallock, 2008, 2010; Söyler *et al.*, 2009; Vekhov and Hallock, 2012; Cheng *et al.*, 2015; Cheng and Beamish, 2016; Matsuda *et al.*, 2016; Nomura, Matsuda, and Okuda, 2019; Shin and Chan, 2019). The spontaneous formation of droplets is expected to modify the elastic
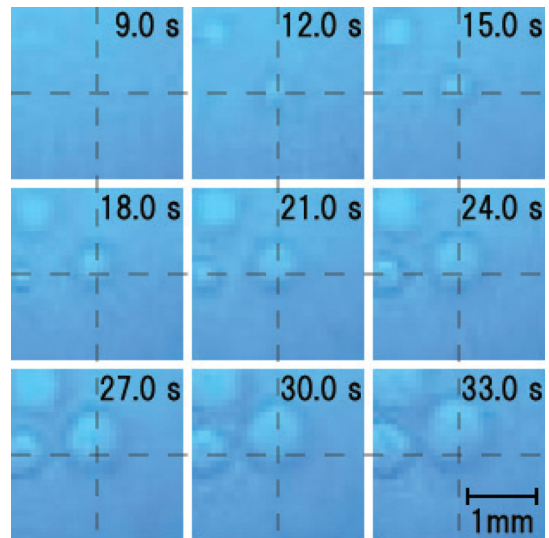


FIG. 18. Spontaneous formation and growth of superfluid droplets inside a ${}^4$He crystal on cooling. The time is indicated in each frame. The initial temperature was 1.65 K. Initially, there was no sign of droplets, but suddenly three droplets appeared and enlarged in the host crystal. They grew to about 1 mm in diameter in about 20 s. From Takahashi, Nomura, and Okuda, 2012a.

property of the host crystal and could cause its anomalous response to shear stress (Sausset, Biroli, and Kurchan, 2010). A video clip of Fig. 18 is provided in the Supplemental Material (161) as movieFig18.

## VII. ASYMMETRY IN MELTING AND GROWTH RELAXATIONS OF ⁴He CRYSTALS

"Which is faster, melting or growth?" is a fundamental question in crystal growth physics. When the intrinsic mobility of the interface, not diffusion in the bulk phase, controls the rate of the phase transitions, it is reasonable to expect that both processes proceed at a similar rate. On the contrary, it has been reported that melting is faster than growth (Weeks and Gilmer, 1979; Amrit and Bossy, 1993; Nomura *et al.*, 1994; Kawaguchi *et al.*, 2002). It is generally observed that the melting process is dominated by fast-moving rough surfaces, and that the growth process is limited by slow facet motion (Elbaum and Wettlaufer, 1993; Maruyama *et al.*, 2000). Therefore, the melting shape of crystals is usually formed by rough surfaces, whereas the growth shape is formed by facets, as mentioned in Sec. II. It is not easy to compare the melting and growth velocities of a particular interface of crystals because the crystal morphologies in melting and growth are sometimes significantly different, as in Figs. 1(c) and 1(d). Acoustic radiation pressure is a useful driving force that can manipulate a particular surface of a desired orientation of a ⁴He crystal locally and allows the difference in melting and growth to be investigated in a controlled manner (Nomura, Abe, and Okuda, 2017). After manipulation by an acoustic wave pulse, the melting relaxation was found to be much slower than the growth relaxation for a $c$ facet and its vicinal surface. The melting relaxation had a complicated behavior with multiple stages, showing anomalous shapes depending on temperature, while the growth relaxation simply returned the crystal to the initial flat surface in a single stage. This asymmetry in melting and growth is not evident for rough surfaces.

An ultrasound pulse was applied to a crystal surface to manipulate it by acoustic radiation pressure and the relaxation process after the pulse was turned off was examined. Two ultrasound transducers were installed in the upper and lower parts of the sample cell facing each other. Their separation was 10 mm and the effective diameter was about 5 mm. The acoustic wave direction was vertical. The procedure of the experiment is as follows. A crystal of a particular orientation is prepared filling the lower space of the cell, and the position of the crystal-superfluid interface is adjusted to be around midway between the two transducers. The lower transducer was buried in the crystal. The interface became horizontally flat due to gravity, and the acoustic waves could propagate perpendicular to the interface. An acoustic wave pulse was applied from one of the two transducers to the interface to induce crystallization or melting.

During the application of the acoustic wave pulse from the lower transducer, the crystal grew largely in the region where the acoustic wave hit and relaxed to a horizontal surface after the pulse was turned off, as shown in Fig. 19. The temperature was 0.5 K and the pulse width was 50 ms. The orientation of the $c$ facet was nearly horizontal in this case. The temporal
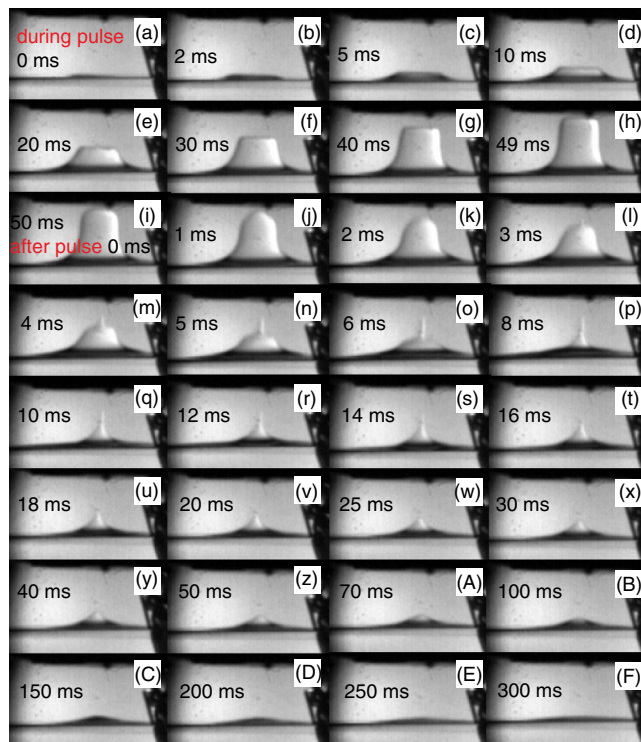


FIG. 19. (a)–(i) Crystallization of a ⁴He crystal by an upward acoustic radiation pressure pulse and (j)–(F) melting relaxation after the pulse was turned off. The elapsed time is indicated in each frame. The temperature was 0.5 K. The orientation of the $c$ facet was nearly horizontal. The width of each frame is 9.5 mm. From Nomura, Abe, and Okuda, 2017.

evolution of the crystal shape was recorded by a high-speed video camera. A clear $c$ facet appeared on the top of the growth part of the crystal during the pulse, as shown in Figs. 19(a)–19(i). The appearance of the facet is a general feature of the growth shape.

The melting relaxation process from the largely deformed crystal is shown in Figs. 19(i)–19(F), after the acoustic wave pulse was turned off. The first observation is that the sharp facet edge rounded quickly via local melting; it melted by approximately 0.5 mm during the first 1 ms and the crystal became a bell-like shape within a few milliseconds [Figs. 19(j) and 19(k)]. This melting velocity $v$ reached as high as $v = 50$ cm/s, which should emit a local superflow of velocity $v_L = \Delta\rho v / \rho_L \approx$ 5 cm/s. The shoulder of the bell-shaped crystal continued to melt [Figs. 19(l)–19(q)] for 10 ms, and a needlelike shape appeared in the center at 3 ms [Fig. 19(l)]. The needle shape was prominent at 8 ms [Fig. 19(p)] and became shorter at around 20 ms [Fig. 19(v)]. The remaining pointed shape stably survived for a longer period and finally disappeared at 300 ms [Fig. 19(F)]. The melting relaxation consisted of two stages. In the first stage, the facet quickly disappeared and the bell shape formed [Figs. 19(i)–19(k)]. In the second stage, the needle shape appeared in the center and became gradually shorter while relaxing to a horizontal shape [Figs. 19(l)–19(F)]. A video clip of Fig. 19 is provided in the Supplemental Material (161) as movieFig19.

Figure 20 shows the case of an acoustic wave in the opposite direction. The manipulation pulse was sent from the
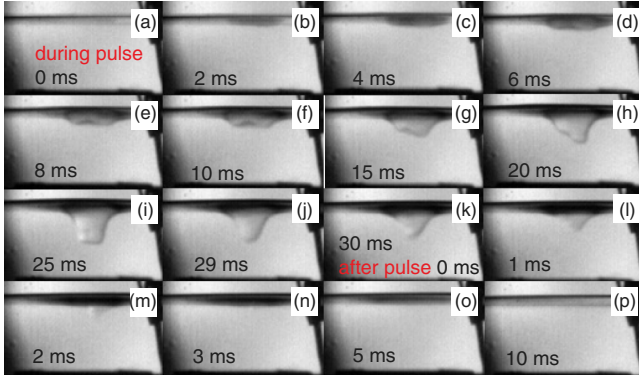
FIG. 20. (a)–(k) Melting of a $^4$He crystal by a downward acoustic radiation pressure pulse and (l)–(p) growth relaxation after the pulse was turned off. The elapsed time is indicated in each frame. The temperature was 0.5 K. The orientation of the $c$ facet was nearly horizontal. The width of each frame is 10.2 mm. From Nomura, Abe, and Okuda, 2017.

upper transducer to induce melting, and the growth relaxation is shown after the pulse was turned off. The temperature was 0.5 K and the pulse width was 30 ms. In Figs. 20(a)–20(k), the crystal was melted by an acoustic wave pulse. A $c$ facet was observed while the acoustic wave pulse was applied, even for the melting shape, though it was not as stable as the growth shape in Fig. 19 and fluctuated during the pulse. After the pulse was turned off, the crystal relaxed to a horizontal surface within 10 ms via crystal growth [Figs. 20(k)–20(p)]. The growth relaxation was simple, occurring in a single stage, and was much faster than the melting relaxation shown in Fig. 19. No anomalous shape, such as a needlelike shape, was observed during the growth relaxation. A video clip of Fig. 20 is provided in the Supplemental Material (161) as movieFig20.

It was found that in the relaxation process to the equilibrium shape the melting was much slower than growth for a $^4$He crystal with a nearly horizontal $c$ facet. The melting relaxation after a large deformation progressed in two stages with complicated behavior, whereas the growth relaxation progressed in a single stage with simple behavior. A needle shape appears in the melting relaxation with a high curvature and thus a higher energy than the lower curvature shape appearing in the growth relaxation. However, the high curvature state in Fig. 19 relaxed much slower than the low curvature state in Fig. 20. This is the opposite of the previously mentioned expectation from the energetics of the curvature. To explain this unexpected asymmetry, a mechanism is required to stabilize the crystal phase and slow down the melting relaxation.

Since the flow profiles are significantly different in the melting and growth relaxations, an asymmetric relaxation can arise in an induced superflow during the relaxation. The flowing liquid has a higher energy than the liquid at rest, so the crystal is more stable when it has a liquid with flow around, as examined next.

Suppose that an interface is lifted with a displacement $h$, creating a local curvature $C$, and that a superfluid flows parallel to the interface with a velocity of $v_L$. The chemical potential difference between the crystal and the superfluid

liquid $\Delta\mu$ can be expressed as a sum of three factors as (Uwaha and Nozières, 1986; Parshin, 1995)

$$\Delta\mu = \Delta\mu_g + \Delta\mu_C + \Delta\mu_f = -\frac{\Delta\rho g h}{\rho_C} - \frac{\alpha C}{\rho_C} + \frac{1}{2}v_L^2. \quad (15)$$

Here the first term denotes the gravitational energy, the second term is the surface energy, and the third term is the kinetic energy of the superflow. Crystallization (melting) is induced when $\Delta\mu > (<) 0$. It is notable that $\Delta\mu_g$ and $\Delta\mu_C$ change their signs depending on the signs of $h$ and $C$, while $\Delta\mu_f > 0$ always holds if a flow exists. This asymmetric contribution can be a source of asymmetric relaxation.

For growth relaxation, $h < 0$ and $C < 0$, and thus $\Delta\mu_g > 0$, $\Delta\mu_C > 0$, and $\Delta\mu_f > 0$. Therefore, the superflow accelerates the growth relaxation. For melting relaxation, $h > 0$ and $C > 0$, and thus $\Delta\mu_g < 0$ and $\Delta\mu_C < 0$, whereas $\Delta\mu_f > 0$. Therefore, $|\Delta\mu|$ is smaller in the presence of a superflow, and the melting relaxation should then be slower. Consequently, the presence of a superflow qualitatively explains the asymmetric relaxation if the superflow velocity is high enough.

A typical displacement and curvature observed in the second stage of Fig. 19(z) was $h \approx 0.1$ cm and $C \approx 10$ cm$^{-1}$, corresponding to $\Delta\mu_g \approx \Delta\mu_C \approx -10$ cm$^2$/s$^2$. If these are compensated for by a superflow, $v_L \approx 6$ cm/s is required in Eq. (15) to make $|\Delta\mu| = 0$. The observed maximum interface velocity was $v = 50$ cm/s in the first stage [Figs. 19(i)–19(k)] and the induced superfluid velocity is estimated to be $v_L \approx 5$ cm/s, which is comparable to 6 cm/s.

A schematic illustration of the crystal shape during melting relaxation and a possible flow profile are shown in Fig. 21. The quick disappearance of the sharp facet edge [the circles in Fig. 21(a)] in the first stage and the formation of the bell shape in Fig. 21(b) can be understood as being due to the facet edge having a high curvature. Such a high curvature shape has a high surface energy and should be unstable without an acoustic radiation pressure field, and thus it should become rounded quickly. The initial superflow fields must be normal to the moving interfaces, expanding radially from the facet edge, as indicated by the arrows in Fig. 21(b). Provided that
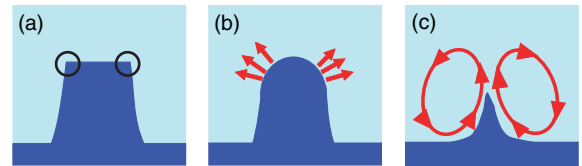


FIG. 21. Schematic illustrations of a crystal surface during melting relaxation. (a) A clear $c$ facet appeared in the growth shape while the acoustic radiation pressure pulse was applied. The facet edge is indicated by the circles. (b) Quick rounding of the sharp facet edge and appearance of a bell shape after the pulse was turned off. The local superflow was emitted normal to the melting crystal surface and expanded radially from the facet edge, as indicated by the arrows. (c) Needle shape and hypothetical subsequent superflow streamlines parallel to the interface. A superfluid flow velocity of as high as 6 cm/s explains the slow relaxation in the second stage of melting relaxation, reducing $|\Delta\mu|$; see the text. From Nomura, Abe, and Okuda, 2017.

the initial high-velocity superflow developed into an almost stationary flow with a velocity parallel to the interface of the order of 6 cm/s, as shown in Fig. 21(c), a slow relaxation would occur in the second stage of melting due to the smaller $|\Delta\mu|$. Such a flow profile has a macroscopic vorticity that should consist of aligned quantized vortices.

A sharp facet edge appeared when the acoustic wave was applied to a crystal with a nearly horizontal *c* facet. This resulted from the crystalline anisotropy, which is most prominent on the surfaces near the facet. On the rough surfaces, however, such a sharp feature did not show up due to their isotropy. The deformation induced by the acoustic pulse was rather rounded. Therefore, no high-velocity superflow was induced and the crystal was not stable enough for the rough surfaces. This superflow model can explain the absence of asymmetric relaxation on rough surfaces.

This superflow model can qualitatively explain the asymmetric relaxation, but it should be noted that the model assumes that the superfluid flow survives during the relaxation process. To draw a final conclusion, the survival of such a superflow should be confirmed by follow-up experiments or simulation studies.

## VIII. INSTABILITIES ON $^4$He CRYSTAL SURFACES

The fluttering motion of the crystal surface observed for disturbed falling in Fig. 11 is likely to be Kelvin-Helmholtz instability induced by the surrounding superflow along the surface. The facets were found to be more stable than the rough surfaces against the instability.

Here we mention three new examples of instability of $^4$He crystal surfaces. The first two are the instability observed after a large deformation by acoustic radiation pressure and that when a growing crystal touches a wall. The third is the Faraday instability of crystallization waves.

### A. After manipulation by acoustic radiation pressure

When there exists a relative flow along an interface between two fluids, the flat interface becomes unstable and corrugated. This is called Kelvin-Helmholtz instability and should be observable in both classical and quantum fluids (Blaauwgeers *et al.*, 2002; Takeuchi *et al.*, 2010; Baggaley and Parker, 2018). A similar instability was predicted on $^4$He crystal surfaces when a superfluid flows parallel to a horizontal flat crystal surface (Uwaha and Nozières, 1986). When the flow velocity exceeds a critical velocity, the flat crystal surface should become unstable and corrugated. This is Kelvin-Helmholtz instability of the crystal surface. Its critical velocity on rough surfaces was estimated to be

$$v_c = \sqrt[4]{\frac{4\alpha g\Delta\rho}{\rho_L^2}} = 4 \text{ cm/s}. \qquad (16)$$

The wavelength of the corrugation should be $l_c$, which is the capillary length defined previously.

Using the same experimental setup as in Sec. VII, we observed irregular shapes of a $^4$He crystal at lower temperatures in the melting relaxation after growth by an acoustic
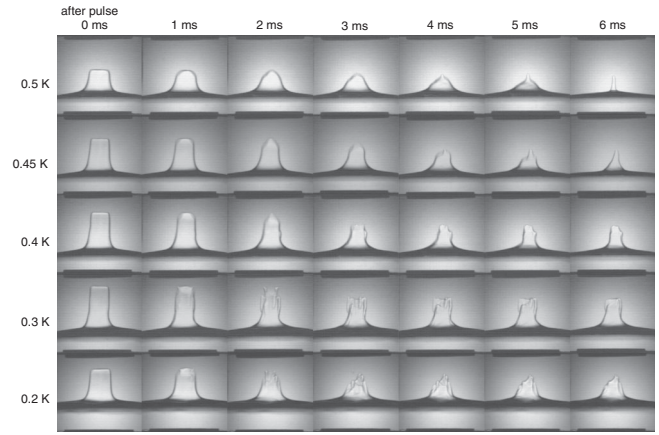


FIG. 22. Melting relaxation of a $^4$He crystal after crystallization by an upward acoustic radiation pressure pulse. The width of each frame is 10 mm. The relaxation shapes at 0.5, 0.45, 0.4, 0.3, and 0.2 K are shown as lines. The elapsed time after the pulse is indicated in the vertical columns (0–6 ms). At 0.5 K, the shape was bell-like at 2–4 ms and needlelike at 6 ms. On the other hand, below 0.4 K it was more irregular, and fingerlike structures appeared at 2–4 ms. From Nomura, Abe, and Okuda, 2017.

radiation pressure pulse. Below 0.4 K, the irregular shape became more distinct; a fingerlike shape appeared at 2–4 ms, as shown in Fig. 22, while it was smoother and bell-like at 0.5 K. The appearance of the irregular shape indicates an occurrence of interface instability (Nomura, Abe, and Okuda, 2017).

The initial superflow from 0 to 1 ms had a velocity of $v_L = 5$ cm/s, evaluated from the interface velocity. The maximum velocity of $v_L = 20$ cm/s was realized from 2 to 3 ms, below 0.4 K, which was well beyond $v_c$. Therefore, it is possible that Kelvin-Helmholtz instability occurred during the relaxation and caused the fingerlike crystal shape. The irregular shape was more distinct at lower temperatures because the interface mobility was higher, inducing a more violent superflow.

### B. When touching a wall

When a $^4$He crystal touches a wall, it should relax to a new equilibrium shape under the new boundary condition set by the wall. In the presence of the wall, the shape before the contact can be regarded as a shape far from equilibrium, as is the case of a strongly deformed crystal by acoustic radiation pressure, and thus its relaxation process is expected to show a curious behavior. This situation was realized when a $^4$He crystal grew slowly from above toward the bottom wall and finally touched the bottom (Abe *et al.*, 2008).

The experimental procedure was as follows. A $^4$He crystal was nucleated on the lower side of the transducer by an acoustic wave pulse. The seed crystal was grown slowly by supplying $^4$He to the cell while keeping the crystal attached to the transducer. The crystal grew downward at a velocity of $v = 0.6$ mm/s and eventually touched the bottom wall. The velocity was 2 orders of magnitude lower than that of the collision discussed in Sec. V. The crystal had a hexagonal shape at 0 ms, as shown in Fig. 23, which was the growth
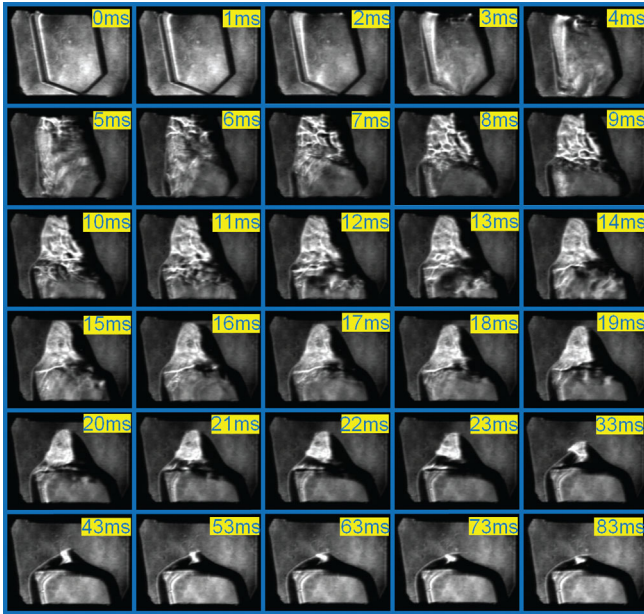
FIG. 23. Deformation of a $^4$He crystal when it touched the bottom of the cell. The elapsed time is indicated in each frame. The temperature was 0.23 K. The crystal was initially stuck on the top of the cell and grew slowly. It eventually touched the bottom without detaching from the top, quickly transformed its shape to adjust to the new boundary condition, and settled on the bottom. During the transformation a corrugation appeared on the surface from 5 to 13 ms, which is an indication of the instability of the smooth surface. The frame size is 15 mm in width.

shape completely covered by facets. The $c$ facet was nearly parallel to the vertical, facing the observation direction. The distance between the transducer and the bottom was 10 mm. The image was taken by a high-speed video camera with the schlieren technique (Settles, 2001) to visualize small changes in the refraction.

Figure 23 shows the moment at 3 ms when the crystal touched the bottom wall. The contact angle between a $^4$He crystal and the wall is about 135° (Sasaki, Caupin, and Balibar, 2008), so it quickly transformed into a new shape due to the driving force of the wettability in order to adjust to the new boundary condition. The contact region with the bottom wall expanded rapidly via crystallization at the maximum interface velocity of $v \simeq 3$ m/s during 2–4 ms. Simultaneously, the contact region with the upper transducer shrank via melting to conserve the crystal volume at a slightly lower velocity of $v \simeq 1$ m/s. This crystallization in the lower part and melting in the upper part should have induced a downward superflow with a velocity of the order of $v_L = \Delta\rho v / \rho_L \sim 10$ cm/s. The original facets disappeared and the crystal shape was more rounded at 5 ms. Thereafter, the facets reappeared from the bottom during 5–10 ms. Corrugation on the surface, which was visualized as a sharp brightness contrast in the schlieren image, appeared in the upper part of the crystal over 5–13 ms. The wavelength of the corrugation was of the order of 1 mm. During this time period, the interface velocity was still high at $v \simeq 1$ m/s. The upper part of the crystal became thinner and eventually detached from the transducer at 16 ms. The upper rough part slowly

shrank and disappeared at around 130 ms and finally the facets covered the surface again. A video clip of Fig. 23 is provided in the Supplemental Material (161) as movieFig23.

The corrugation appeared only transiently and disappeared at around 17 ms and thus is not due to the crystal defects discussed by Sasaki, Caupin, and Balibar (2008) but is instead due to an instability on the surface. The superfluid flow during the transformation had a high velocity and flowed mostly parallel to the crystal surface toward the bottom. Therefore, Kelvin-Helmholtz instability is likely the origin of the observed corrugation. Equation (16) is the critical velocity for a horizontal surface and cannot be applied in the present case where the surface was nearly vertical. Provided that $g$ in Eq. (16) can be simply replaced with the effective gravity $g \sin\theta$, $v_c$ can be reduced and thus the instability should occur more easily even under a more gentle flow. Here $\theta$ is the angle of the interface measured from the vertical direction. The estimated flow velocity $v_L = 10$ cm/s was high enough to induce Kelvin-Helmholtz instability on the nearly vertical crystal surface.

Although the corrugation appeared on the surface, no propagation of a crystallization wave was observed, in contrast to the collision in Fig. 9. This difference indicates that the earlier kinetic energy of the crystal including that of the surrounding superflow influences the dynamics when touching or colliding with a wall.

### C. Faraday instability

When the gravity acceleration is modulated at an angular frequency of $2\omega$ or, equivalently, a container of fluid is oscillated at $2\omega$, a flat surface of the fluid becomes unstable and standing waves are parametrically excited on the fluid surface at a frequency $\omega$. This phenomenon is called Faraday instability (Faraday, 1831; Cross and Hohenberg, 1993), which is found in both classical fluids and superfluids (Abe *et al.*, 2007a; Engels, Atherton, and Hoefer, 2007; Levchenko, Mezhov-Deglin, and Pel'menev, 2017; Nguyen *et al.*, 2019). It was predicted that such instability would occur on a $^4$He crystal surface when $K(T)$ is large enough at low temperatures (van Saarloos and Weeks, 1995). It was shown that displacement of the superfluid-crystal interface $\xi$ from the equilibrium flat position follows the Mathieu equation

$$\ddot{\xi}_k + \Gamma_k \dot{\xi}_k + \omega_0^2(k)[1 + 2\epsilon \cos 2\omega t]\xi_k = 0, \qquad (17)$$

where $\Gamma_k = \rho_C \rho_L k / K(T)(\Delta\rho)^2$, $\omega_0(k)$, and $\epsilon$ are the damping coefficient, the frequency of the crystallization wave at the wave number $k$, and the scaled driving amplitude, respectively. A flat interface becomes unstable and standing waves develop on the crystal surface above a critical driving amplitude

$$\tilde{\epsilon}_c = \frac{4A_c \omega^2}{g} = \frac{2\rho_C \omega}{K(T)g\Delta\rho} \qquad (18)$$

at $\omega = \omega_0(k)$. Here $A_c$ is the critical oscillation amplitude of the container. Measurements of the critical amplitude can be used as a new method to determine $K(T)$. The dissipation

takes place on the surface for the crystallization wave, while it is due to the viscosity in the bulk for a simple fluid case. It is of interest to determine what kind of instability patterns will develop on crystal surfaces with the anisotropic surface energy compared with fluid surfaces that are intrinsically isotropic.

An experiment was conducted in a sample cell which was oscillated vertically by an electrical drive (Abe *et al.*, 2007a). A large ⁴He crystal was grown in the cell to occupy the lower part of the cell. The crystal-superfluid interface was horizontally flat due to gravity. A mirror was installed over the interface in the cell to get a reflection from the interface through a side window by a high-speed video camera. The brightness $I$ at a particular point in the high-speed image was fast Fourier transformed to obtain the spectra of the excited crystallization waves.

Fourier spectra of the excited crystallization waves are shown in Fig. 24(a). The measurements were done at 170 mK and the driving frequency was $f_d = 92$ Hz (Abe *et al.*, 2007b). It can be seen that the wave had a subharmonic component at $f_d/2$ and thus a Faraday wave was parametrically excited. The peak at $f_d/2$ did not appear for a low driving amplitude but did appear above a critical driving amplitude. Figure 24(b) shows the temperature dependence of the peak height at $f_d/2$ with a constant driving amplitude. Faraday waves became smaller at higher temperatures, disappearing above 200 mK, which is consistent with the temperature dependence of $K(T)$. The large error bars at low temperatures were due to the significant heating during the oscillations.

Faraday instability occurred only at extremely low temperatures, making a systematic measurement difficult. The critical amplitude was roughly estimated to be of the order of a few 0.1 $\mu$m at around 170 mK, but accurate calibration of such a small displacement was not possible. The critical amplitude might be temperature dependent, but this is not known for certain currently. Since we could visually observe only a part of the whole interface, the excited modes have not yet been successfully identified. The experimental investigation is still preliminary, though Faraday instability of the crystal surface has been confirmed. Consequently, ⁴He cr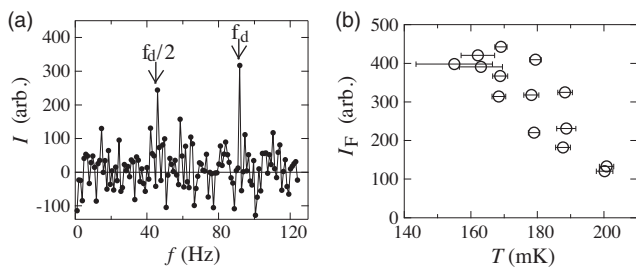ystals have been shown to be a promising system for studying hydrodynamic instabilities of anisotropic surfaces and for searching for new instability patterns that have not been observed in isotropic fluid systems.

## IX. TRANSVERSE MOTIONS OF A ⁴He CRYSTAL

Moving a ⁴He crystal in a superfluid is challenging. While slippage of two-dimensinal ⁴He crystals is known to occur on graphite surfaces (Hieda *et al.*, 2000; Hosomi *et al.*, 2009), there are no known means of moving macroscopic ⁴He crystals in a well-controlled manner. It was demonstrated that a ⁴He crystal can undergo a transverse motion on an asymmetrically oscillating plate (Yoshida *et al.*, 2017). This method is called inchworm driving and is used to impart motion to classical solid objects employing the difference between static and dynamic friction forces. This method also works for ⁴He crystals in superfluid liquid, but the observed motion of ⁴He crystals was quite different from the ordinary behavior of classical objects.

Experiments were performed in a similar high-pressure cell with optical windows. A piezoelectric driving device was installed in the sample cell and a stainless steel plate was glued to a piezoelectric ceramic post made of layered lead zirconate titanate. The piezoelectric post was driven in a shear mode by applying high voltage. It oscillated in the left and right directions with an amplitude of 0.7 $\mu$m for an applied 300 V at a low temperature of 0.3 K. In the driving, the plate moved slowly over 0.99 ms to the right and returned to the left rapidly over 0.01 ms. We applied 100 asymmetric sawtoothlike oscillation pulses with a repetition period of 10 ms for 1 s. It was expected that the crystal would move to the right.

A seed ⁴He crystal was nucleated and grown on an ultrasound transducer in the upper part of the cell. The crystal eventually detached from the transducer, falling on a horizontal stainless steel plate, as in Sec. V. After several trials, a ⁴He crystal was properly placed on the plate and ready for driving. A $c$ facet of the crystal appeared on the upper surface; crystals landed on the plate with a flat $c$ facet that was horizontal in most cases.

Successful driving of a ⁴He crystal in a superfluid at 0.3 K is shown in Figs. 25(a) and 25(b). Two photographs at 0 and 0.6 s are superimposed in Fig. 25(a). In this initial stage for the first 0.6 s, the crystal did not move but changed its shape; it was initially 3.6 mm in width and 1.1 mm in height. At 0.6 s, it became more rounded without a facet and was 3.0 mm in width and 1.7 mm in height. Note that the right-hand side of the contact line on the plate did not move during this period in Fig. 25(a), which indicates that the crystal did not slip on the plate although the center of mass moved slightly rightward. In Fig. 25(b), two photographs at 0.6 and 1.0 s are also superimposed. The crystal eventually started to move to the right at 0.6 s, keeping the same shape, and stopped at 1.0 s when the pulses were turned off. The distance traversed was 0.27 mm for 40 oscillation pulses over 0.4 s; the crystal moved approximately 7 $\mu$m in response to each pulse. The contact line motion on the plate during the oscillation pulses for 1.0 s is schematically illustrated in Figs. 25(c) and 25(d).

This value of crystal displacement is significantly larger than the oscillation amplitude of the plate, 0.7 $\mu$m. It is conceivable that the present motion of the ⁴He crystal was not

FIG. 24. (a) Fourier spectra of the brightness $I$ of an illuminated ⁴He crystal surface in a vertically oscillating sample cell. The driving frequency $f_d$ was 92 Hz and the temperature was 170 mK. A peak at half of the driving frequency is a clear indication of the parametric driving of Faraday instability of the crystallization waves. (b) Temperature dependence of the amplitude of the excited Faraday waves of a ⁴He crystal with a driving frequency of 92 Hz. The Faraday waves disappeared above 200 mK due to the decrease of $K(T)$ at high temperatures. From Abe *et al.*, 2007b.
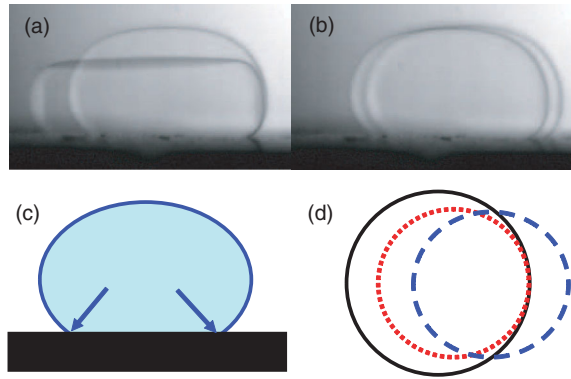
FIG. 25.    (a) Superimposed image of a $^4$He crystal at 0 and 0.6 s. The crystal was placed on a horizontally oscillating plate and 100 sawtoothlike oscillation pulses were applied for 1.0 s. The temperature was 0.3 K. The crystal was initially flat with a horizontal $c$ facet and deformed to be rounded at 0.6 s. (b) Superimposed images of the $^4$He crystal at 0.6 and 1.0 s. The crystal moved to the right, keeping a rounded shape. (c) Schematic side view of the $^4$He crystal. The arrows depict the contact line on the plate. (d) Schematic top view of the contact line and its motion on the plate. The black solid line represents the contact line shape before the oscillations, the red dotted line is the contact line after the initial deformation at 0.6 s, and the blue dashed line is after the motion at 1.0 s. From Yoshida *et al.*, 2017.

due to the simple inchworm driving via a stick and slip process but instead due to a novel mechanism peculiar to the quantum crystal. The initial deformation of the crystal cannot be accounted for by the standard inchworm driving model either.

To explain the peculiarly large motion of the crystal, an exotic mechanism was proposed in Yoshida *et al.* (2017), where the crystallization on the right-hand side and melting on the left-hand side were taken into account. As the plate moved slowly to the right with an amplitude of $d$, the right-hand side of the crystal moving with the plate encountered an incoming superflow. The superflow incident on the crystal-superfluid interface induced crystallization due to the high crystallization rate (Maksimov and Tsymbalenko, 2002; Tsymbalenko, 2013; Nomura *et al.*, 2014). The induced displacement of the interface $d'$ would be increased by 1 order of magnitude as $d' = (\rho_L/\Delta\rho)d \approx 10d$ owing to mass conservation. On the other hand, the left-hand side of the crystal would melt over the same range $d'$ induced by the outgoing superflow. If the crystal stayed at the same position while the plate was quickly moved back to the left, the total movement of the crystal could be 10 times larger than that of the standard model. Thus, a quantum crystal can be moved over much longer distances than a classical object if the fast growth or melting rate of the liquid-solid interface is taken into account in the oscillation process.

To check whether this explanation is plausible, the same experiment should be performed at high temperatures, where the crystallization proceeds much slower. However, the temperature dependence has not been measured yet, and thus the proposed mechanism is not definite. The origin of the overall response to the plate oscillation, the initial deformation, and the following significant motion remain to be determined.

Traversing a macroscopic $^4$He crystal in a superfluid liquid was demonstrated in this experiment. This is a major step for studying the friction between a $^4$He crystal and a wall and between two $^4$He crystals. Tribology is the field of studying the science of wear, friction, and lubrication and has traditionally treated classical objects but not quantum matter such as $^4$He crystals. The tribology of quantum matter or the quantum tribology of $^4$He crystals would provide important insights because quantum effects would emerge, leading to the observation of unknown quantum phenomena in the friction dynamics even on the macroscopic scale, e.g., a depinning motion via macroscopic quantum tunneling.

A video clip of Fig. 25 is provided in the Supplemental Material (161) as movieFig25ab. For reference, video clips of a longer distance motion of $^4$He crystals to the right and to the left by applying a longer driving are also provided in the Supplemental Material (161) as movieFig25_2 and movieFig25_3, respectively.

The contact angles of $^4$He crystals were measured on an artificially roughened surface to demonstrate that the contact angle to the roughened wall was possibly increased (Takahashi *et al.*, 2016). If a spatial modulation of the wettability of a substrate surface is introduced, artificial pinning for a $^4$He crystal would be possible, opening a way to examine the transverse motion of a $^4$He crystal in a more systematic manner.

## X. SUMMARY AND OUTLOOK

In this Colloquium we have described the dynamics of $^4$He crystal shapes when the crystals are placed out of equilibrium. The driving forces that brought the crystals out of equilibrium were unique and are considered to be irrelevant for crystal growth in classical systems, including gravity, superflow, wettability, acoustic waves, container oscillations, frictional forces, and others.

Some of the observed out-of-equilibrium behaviors are not merely a special character of these crystals but should be regarded as being universal and should occur in principle in classical crystals. However, they are concealed by dissipations and are usually considered to be impossible in classical systems because they proceed extremely slowly, over a geological timescale. For example, air bubbles are often formed in an ice crystal in a freezer but do not move upward by buoyancy. They are energetically favored to rise in the ice but the process takes too long for their rising to be recognized. In contrast, quantum crystallization of $^4$He is accelerated by the superfluidity and thus the permitted phenomena will occur even under weak driving forces, including the following. Superfluid droplets forming in a $^4$He crystal do indeed rise by buoyancy. Their motion and shape became anisotropic with cooling, reflecting the roughening transition of the host crystal. Ostwald ripening of crystals crushed by acoustic waves is effected rapidly, in a few seconds under zero gravity even at the macroscopic scale. Crystallization and melting can be selectively induced by a small acoustic force due to radiation pressure. These experiments on $^4$He quantum crystals have provided rare opportunities to visualize these dynamical phenomena *in situ* and should shed light on the unseen parts of the general crystal growth processes.

The parabolic flight experiments realized on a jet plane provided a zero-gravity and ultralow temperature environment, allowing the first observations of gravity-free $^4$He crystals of macroscopic size. $^4$He crystals responded quickly to the sudden reduction of gravity, relaxing to the equilibrium state, which provided important information about the ECS.

Superflow was found to play a significant role in the crystallization far from equilibrium. Superflow drastically deformed the shape of a crystal when it fell in a superfluid and modified the collisional process with a wall and a needle. Anomalous crystal shapes were observed in the relaxation process after deformation by acoustic radiation pressure. The relaxation was influenced by the superflow, induced by a quick surface motion during the relaxation. The superflow probably induced an enhanced transverse movement of the crystal on the asymmetrically oscillating plate. The superflow also caused some instabilities on the crystal surface. These behaviors may be characteristic of the quantum crystallization of $^4$He, which coupled strongly with the concomitant superfluid motion.

These observations should be closely related to more general problems of hydrodynamics and interface instabilities of Bose-condensed fluid systems out of equilibrium, which have drawn increasing interest recently (Abe *et al.*, 2007a; Engels, Atherton, and Hoefer, 2007; Takeuchi *et al.*, 2010; Kobyakov *et al.*, 2011; Kadokura *et al.*, 2012; Tsubota, 2013; Indekeu *et al.*, 2018; Xi, Byrnes, and Saito, 2018; Nguyen *et al.*, 2019). The dynamical properties of such quantum fluids are also governed by the motions of order-parameter fields and quantized vortices, although they are not in contact with a crystalline phase and thus are much more isotropic than a $^4$He crystal-superfluid system.

Most of the observations of the crystallization dynamics could be qualitatively understood considering the effect of superflow. However, the mechanisms proposed here are not yet definite and conclusive, since the superflow profile itself could not be visualized directly. Several flow imaging methods have been developed (Yarmchuk, Gordon, and Packard, 1979; Bewley, Lathrop, and Sreenivasan, 2006; Gordon *et al.*, 2007; Zmeev *et al.*, 2013; Gomez *et al.*, 2014; Moroshkin *et al.*, 2019), but they are currently difficult to apply at extremely low temperatures. Simulation of the superflow profile is another way to determine the origin of the dynamical phenomena of crystal shape and growth. However, this would not be an easy project because both the superfluid hydrodynamics and the crystal-superfluid phase transition need to be taken into account equally. A moving crystal surface sets a time dependent boundary condition and generates superflow. Additionally, the surface free energy and crystal growth rates are orientation dependent, meaning that the crystal surface is highly anisotropic both statically and dynamically. This makes simulation studies much harder than studies of isotropic Bose-condensed superfluids.

However, the occurrence of these peculiar phenomena was definitely observed thanks to visualizations of the crystal shape by the high-speed video camera. Furthermore, the crystal shapes themselves provided important information on the superflow profile, because the superfluid flowed under the restrictions set by the crystal surface and the superflows

were generated by the crystal surface motions. This Colloquium should trigger further challenging theoretical and experimental studies on the cooperative phenomena of the superflow and phase transition of anisotropic quantum matter far from equilibrium.

## REFERENCES

Abe, H., M. Morikawa, T. Ueda, R. Nomura, and Y. Okuda, 2008, J. Low Temp. Phys. **150**, 289.

Abe, H., F. Ogasawara, Y. Saitoh, T. Tatara, S. Kimura, R. Nomura, and Y. Okuda, 2005, Phys. Rev. B **71**, 214506.

Abe, H., Y. Saitoh, T. Ueda, F. Ogasawara, R. Nomura, Y. Okuda, and A. Ya. Parshin, 2006, J. Phys. Soc. Jpn. **75**, 023601.

Abe, H., T. Ueda, M. Morikawa, Y. Saitoh, R. Nomura, and Y. Okuda, 2007a, Phys. Rev. E **76**, 046305.

Abe, H., T. Ueda, M. Morikawa, Y. Saitoh, R. Nomura, and Y. Okuda, 2007b, J. Phys. Conf. Ser. **92**, 012157.

Akutsu, Y., N. Akutsu, and T. Yamamoto, 1988, Phys. Rev. Lett. **61**, 424.

Amrit, J., and J. Bossy, 1993, J. Low Temp. Phys. **92**, 415.

Amrit, J., P. Legros, and J. Poitrenaud, 1995, J. Low Temp. Phys. **101**, 971.

Andreev, A. F., and I. M. Lifshitz, 1969, Sov. Phys. JETP **29**, 1107, http://www.jetp.ac.ru/cgi-bin/e/index/e/29/6/p1107?a=list.

Andreev, A. F., and A. Ya. Parshin, 1978, Sov. Phys. JETP **48**, 763, http://www.jetp.ac.ru/cgi-bin/e/index/e/48/4/p763?a=list.

Andreeva, O. A., and K. O. Keshishev, 1991, Phys. Scr. **T39**, 352.

Avron, J. E., L. S. Balfour, C. G. Kuper, J. Landau, S. G. Lipson, and L. S. Schulman, 1980, Phys. Rev. Lett. **45**, 814.

Babkin, A. V., H. Alles, P. J. Hakonen, A. Ya. Parshin, J. P. Ruutu, and J. P. Saramäki, 1995, Phys. Rev. Lett. **75**, 3324.

Baggaley, A. W., and N. G. Parker, 2018, Phys. Rev. A **97**, 053608.

Balibar, S., H. Alles, and A. Ya. Parshin, 2005, Rev. Mod. Phys. **77**, 317.

Balibar, S., and B. Castaing, 1980, J. Phys. (Paris), Lett. **41**, 329.

Balibar, S., X. Chavanne, and F. Caupin, 2003, Physica (Amsterdam) **329B–333B**, 380.

Balibar, S., and P. Nozières, 1994, Solid State Commun. **92**, 19.

Bewley, G. P., D. P. Lathrop, and K. R. Sreenivasan, 2006, Nature (London) **441**, 588.

Birchenko, A. P., N. P. Mikhin, E. Y. Rudavskii, S. N. Smirnov, and Y. Y. Fysun, 2018, J. Low Temp. Phys. **44**, 304.

Bishop, D. J., and J. D. Reppy, 1978, Phys. Rev. Lett. **40**, 1727.

Blaauwgeers, R., V. B. Eltsov, G. Eska, A. P. Finne, R. P. Haley, M. Krusius, J. J. Ruohio, L. Skrbek, and R. G. Volovik, 2002, Phys. Rev. Lett. **89**, 155301.

Bodensohn, J., K. Nicolai, and P. Leiderer, 1986, Z. Phys. B **64**, 55.

Borgnis, F. E., 1953, Rev. Mod. Phys. **25**, 653.

Bowley, R. M., and D. O. Edwards, 1983, J. Phys. (Paris) **44**, 723.

Brillouin, L., 1925, Ann. Phys. (Paris) **10**, 528.

Burton, W. K., N. Cabrera, and F. C. Frank, 1951, Phil. Trans. R. Soc. A **243**, 299.

Castaing, B., S. Balibar, and C. Laroche, 1980, J. Phys. (Paris) **41**, 897.

Castaing, B., and P. Nozières, 1980, J. Phys. (Paris) **41**, 701.

Chavanne, X., S. Balibar, and F. Caupin, 2001, Phys. Rev. Lett. **86**, 5506.

Cheng, Z. G., and J. Beamish, 2016, Phys. Rev. Lett. **117**, 025301.

Cheng, Z. G., J. Beamish, A. D. Fefferman, F. Souris, S. Balibar, and V. Dauvois, 2015, Phys. Rev. Lett. **114**, 165301.

Chester, G. V., 1970, Phys. Rev. A **2**, 256.

Cross, M. C., and P. C. Hohenberg, 1993, Rev. Mod. Phys. **65**, 851.

Dash, J. G., and J. S. Wettlaufer, 2005, Phys. Rev. Lett. **94**, 235301.

de Gennes, P. G., F. Brochard-Wyart, and D. Quéré, 2004, *Capillarity and Wetting Phenomena: Drops, Bubbles, Pearls, Waves* (Springer, New York).

Elbaum, M., and J. S. Wettlaufer, 1993, Phys. Rev. E **48**, 3180.

Engels, P., C. Atherton, and M. A. Hoefer, 2007, Phys. Rev. Lett. **98**, 095301.

Faraday, M., 1831, Phil. Trans. R. Soc. London **121**, 299.

Fujimoto, K., R. Hamazaki, and M. Ueda, 2018, Phys. Rev. Lett. **120**, 073002.

Gallet, F., S. Balibar, and E. Rolley, 1987, J. Phys. (Paris) **48**, 369.

Gomez, L. F., *et al.*, 2014, Science **345**, 906.

Gordon, E. B., R. Nishida, R. Nomura, and Y. Okuda, 2007, JETP Lett. **85**, 581.

Graf, M. J., and H. J. Maris, 1987, Phys. Rev. B **35**, 3142.

Grinfeld, M. A., 1986, Sov. Phys. Dokl. **31**, 831.

Grinfeld, M. A., 1993, J. Nonlinear Sci. **3**, 35.

Hieda, M., T. Nishino, M. Suzuki, N. Wada, and Y. Torii, 2000, Phys. Rev. Lett. **85**, 5142.

Hofmann, J., S. S. Natu, and S. Das Sarma, 2014, Phys. Rev. Lett. **113**, 095702.

Hoshi, T., Y. Ochiai, and J. Rekimoto, 2014, Jpn. J. Appl. Phys. **53**, 07KE07.

Hosomi, N., J. Taniguchi, M. Suzuki, and T. Minoguchi, 2009, Phys. Rev. B **79**, 172503.

Indekeu, J. O., N. V. Thu, C. Y. Lin, and T. H. Phat, 2018, Phys. Rev. A **97**, 043605.

Ishiguro, R., F. Caupin, and F. Balibar, 2006, Europhys. Lett. **75**, 91.

Ishiguro, R., F. Graner, E. Rolley, and S. Balibar, 2004, Phys. Rev. Lett. **93**, 235301.

Ishiguro, R., F. Graner, E. Rolley, and S. Balibar and J. Eggers, 2007, Phys. Rev. E **75**, 041606.

Jayaprakash, C., W. F. Saam, and S. Teitel, 1983, Phys. Rev. Lett. **50**, 2017.

Kadokura, T., T. Aioi, K. Sasaki, T. Kishimoto, and H. Saito, 2012, Phys. Rev. A **85**, 013602.

Kagan, M. Y., 1986, Sov. Phys. JETP **63**, 288.

Kagiwada, R. S., J. C. Fraser, I. Rudnick, and D. Bergman, 1969, Phys. Rev. Lett. **22**, 338.

Kawaguchi, Y., T. Ueno, Y. Kinoshita, Y. Sasaki, and T. Mizusaki, 2002, J. Low Temp. Phys. **126**, 27.

Keshishev, K. O., and D. B. Shemyatikhin, 2008, J. Low Temp. Phys. **150**, 282.

Keshishev, K. O., A. Ya. Parshin, and A. V. Babkin, 1981, Sov. Phys. JETP **53**, 362.

Keshishev, K. O., A. Ya. Parshin, and A. V. Babkin, 1979, JETP Lett. **30**, 56, http://jetpletters.ac.ru/ps/1361/article_20583.pdf.

Kobyakov, D., V. Bychkov, E. Lundh, A. Bezett, V. Akkerman, and M. Marklund, 2011, Phys. Rev. A **83**, 043623.

Kosevich, A. M., and Y. A. Kosevich, 1981, Fiz. Nizk. Temp. **7**, 809 [Sov. J. Low Temp. Phys. **7**, 394 (1981)].

Kosterlitz, J. M., and D. J. Thouless, 1973, J. Phys. C **6**, 1181.

Landau, L. D., 1965, *Collected Papers* (Pergamon, Oxford).

Landau, L. D., and E. M. Lifshitz, 1987, *Fluid Mechanics* (Pergamon, Oxford).

Leggett, A. J., 1970, Phys. Rev. Lett. **25**, 1543.

Leggett, A. J., 2003, Prog. Surf. Sci. **74**, 405.

Levchenko, A. A., L. P. Mezhov-Deglin, and A. A. Pel'menev, 2017, JETP Lett. **106**, 252.

Lifshitz, I. M., and V. V. Slyozov, 1961, J. Phys. Chem. Solids **19**, 35.

Lipson, S. G., and E. Polturak, 1987, in *Progress in Low Temperature Physics*, Vol. 11, edited by D. F. Brewer (Elsevier, New York), p. 127.

Maksimov, L. A., and V. L. Tsymbalenko, 2002, J. Exp. Theor. Phys. **95**, 455.

Marchenko, V. I., and A. Ya. Parshin, 1980, Sov. Phys. JETP **52**, 129, http://www.jetp.ac.ru/cgi-bin/dn/e_052_01_0129.pdf.

Maris, H. J., 2003, Phys. Rev. E **67**, 066309.

Martin Trusler, J. P., 2011, J. Phys. Chem. Ref. Data **40**, 043105.

Maruyama, M., N. Kuribayashi, K. Kawabata, and J. S. Wettlaufer, 2000, Phys. Rev. Lett. **85**, 2545.

Marzo, A., S. A. Seah, B. W. Drinkwater, D. R. Sahoo, B. Long, and S. Subramanian, 2015, Nat. Commun. **6**, 8661.

Matsuda, H., A. Ochi, R. Isozaki, R. Masumoto, R. Nomura, and Y. Okuda, 2013, Phys. Rev. E **87**, 030401(R).

Matsuda, H., A. Ochi, R. Isozaki, S. Minami, R. Nomura, J. Pollanen, W. P. Halperin, and Y. Okuda, 2016, Phys. Rev. B **94**, 024509.

Mizusaki, T., R. Nomura, and M. Hiroi, 2007, J. Low Temp. Phys. **149**, 143.

Moroshkin, P., P. Leiderer, K. Kono, S. Inui, and M. Tsubota, 2019, Phys. Rev. Lett. **122**, 174502.

Mukai, M., and M. Uwaha, 2006, J. Phys. Soc. Jpn. **75**, 054601.

Nakaya, U., 1954, *Snow Crystals—Natural and Artificial* (Harvard University Press, Cambridge, MA).

Nakaya, U., 1956, SIPRE Research Report No. 13.

Nelson, D. R., and J. M. Kosterlitz, 1977, Phys. Rev. Lett. **39**, 1201.

Nelson, R. S., D. J. Mazey, and R. S. Barnes, 1965, Philos. Mag. **11**, 91.

Nguyen, J. H. V., M. C. Tsatsos, D. Luo, A. U. J. Lode, G. D. Telles, V. S. Bagnato, and R. G. Hulet, 2019, Phys. Rev. X **9**, 011052.

Nomura, R., H. Abe, and Y. Okuda, 2017, New J. Phys. **19**, 023049.

Nomura, R., H. H. Hensley, T. Matsushita, and T. Mizusaki, 1994, J. Low Temp. Phys. **94**, 377.

Nomura, R., S. Kimura, F. Ogasawara, H. Abe, and Y. Okuda, 2004, Phys. Rev. B **70**, 054516.

Nomura, R., H. Matsuda, R. Masumoto, K. Ueno, and Y. Okuda, 2011, J. Phys. Soc. Jpn. **80**, 123601.

Nomura, R., H. Matsuda, and Y. Okuda, 2018, J. Phys. Soc. Jpn. **87**, 115001.

Nomura, R., H. Matsuda, and Y. Okuda, 2019, J. Phys. Soc. Jpn. **88**, 035003.

Nomura, R., A. Osawa, T. Mimori, K. Ueno, H. Kato, and Y. Okuda, 2008, Phys. Rev. Lett. **101**, 175703.

Nomura, R., Y. Suzuki, S. Kimura, and Y. Okuda, 2003, Phys. Rev. Lett. **90**, 075301.

Nomura, R., T. Yoshida, A. Tachiki, and Y. Okuda, 2014, New J. Phys. **16**, 113022.

Nozières, P., 1992, in *Solids Far from Equilibrium*, edited by C. Godrèche (Cambridge University Press, Cambridge, England), p. 1.

Nozières, P., and M. Uwaha, 1987, J. Phys. (Paris) **48**, 389.

Okuda, Y., and R. Nomura, 2008, J. Phys. Soc. Jpn. **77**, 111009.

Okuda, Y., S. Yamazaki, T. Yoshida, H. Fujii, and K. Matsumoto, 1998, J. Low Temp. Phys. **113**, 775.

Onuki, A., 2007, Phys. Rev. E **75**, 036304.

Oono, Y., and M. Paniconi, 1998, Prog. Theor. Phys. Suppl. **130**, 29.

Ostwald, W., 1900, Z. Phys. Chem., Stoechiom. Verwandtschaftsl. **34**, 495.

Parshin, A. Ya., 1985, in *Low Temperature Physics*, edited by A. S. Borovik-Romanov (Mir, Moscow).

Parshin, A. Ya., 1995, Physica (Amsterdam) **210B**, 383.

Parshin, A. Ya., and V. L. Tsymbalenko, 2003, Pis'ma Zh. Eksp. Teor. Fiz. **77**, 372 [JETP Lett. **77**, 321 (2003)].

Pavlovska, P., and D. Nenow, 1971, J. Cryst. Growth **8**, 209.

Poitrenaud, J., and P. Legros, 1989, Europhys. Lett. **8**, 651.

Polturak, E., I. Schuster, I. Berent, Y. Carmi, S. Lipson, and B. Chabaud, 1995, J. Low Temp. Phys. **101**, 177.

Ray, M. W., and R. B. Hallock, 2008, Phys. Rev. Lett. **100**, 235301.

Ray, M. W., and R. B. Hallock, 2010, Phys. Rev. Lett. **105**, 145301.

Rayleigh, Lord, 1902, Philos. Mag. **3**, 338.

Rolley, E., E. Chevalier, C. Guthmann, and S. Balibar, 1994, Phys. Rev. Lett. **72**, 872.

Rolley, E., C. Guthmann, E. Chevalier, and S. Balibar, 1995, J. Low Temp. Phys. **99**, 851.

Ruutu, J. P., P. J. Hakonen, A. V. Babkin, A. Ya. Parshin, J. S. Penttilä, J. P. Saramäki, and G. Tvalashvili, 1996, Phys. Rev. Lett. **76**, 4187.

Ruutu, J. P., P. J. Hakonen, J. S. Penttilä, A. V. Babkin, J. P. Saramäki, and E. B. Sonin, 1996, Phys. Rev. Lett. **77**, 2514.

Sasa, S., and H. Tasaki, 2006, J. Stat. Phys. **125**, 125.

Sasaki, S., F. Caupin, and S. Balibar, 2008, J. Low Temp. Phys. **153**, 43.

Sasaki, Y., and T. Mizusaki, 1998, J. Low Temp. Phys. **110**, 491.

Sato, M., and T. Fujii, 2001, Phys. Rev. E **64**, 026311.

Sausset, F., G. Biroli, and J. Kurchan, 2010, J. Stat. Phys. **140**, 718.

Settles, G. S., 2001, *Schlieren, and Shadowgraph Techniques* (Springer, Berlin).

Shin, J., and M. H. W. Chan, 2019, Phys. Rev. B **99**, 140502(R).

Söyler, S. G., A. B. Kuklov, L. Pollet, N. V. Prokof'ev, and B. V. Svistunov, 2009, Phys. Rev. Lett. **103**, 175301.

Takahashi, T., H. Minezaki, A. Suzuki, K. Obara, K. Itaka, R. Nomura, and Y. Okuda, 2016, Phys. Rev. E **93**, 052806.

Takahashi, T., R. Nomura, and Y. Okuda, 2012a, J. Phys. Conf. Ser. **400**, 012070.

Takahashi, T., R. Nomura, and Y. Okuda, 2012b, Phys. Rev. E **85**, 030601(R).

Takahashi, T., R. Nomura, and Y. Okuda, 2016, J. Low Temp. Phys. **185**, 295.

Takahashi, T., H. Ohuchi, R. Nomura, and Y. Okuda, 2012, New J. Phys. **14**, 123023.

Takahashi, T., H. Ohuchi, R. Nomura, and Y. Okuda, 2015, Sci. Adv. **1**, e1500825.

Takeuchi, H., 2018, Phys. Rev. A **97**, 013617.

Takeuchi, H., N. Suzuki, K. Kasamatsu, H. Saito, and M. Tsubota, 2010, Phys. Rev. B **81**, 094517.

Teshigawara, R., and A. Onuki, 2008, Europhys. Lett. **84**, 36003.

Todoshchenko, I., 2018, Phys. Rev. B **97**, 134101.

Todoshchenko, I. A., H. Alles, H. J. Junes, M. S. Manninen, and A. Ya. Parshin, 2008, Phys. Rev. Lett. **101**, 255302.

Torii, R. H., and S. Balibar, 1992, J. Low Temp. Phys. **89**, 391.

Tsubota, M., 2013, J. Low Temp. Phys. **171**, 571.

Tsymbalenko, V. L., 1992, J. Low Temp. Phys. **88**, 55.

Tsymbalenko, V. L., 2000, J. Low Temp. Phys. **121**, 53.

Tsymbalenko, V. L., 2013, J. Low Temp. Phys. **171**, 21.

Tsymbalenko, V. L., 2015, Phys. Usp. **58**, 1059.

Tsymbalenko, V. L., 2019, J. Low Temp. Phys. **195**, 153.

Uwaha, M., and P. Nozières, 1985, J. Phys. (Paris) **46**, 109.

Uwaha, M., and P. Nozières, 1986, J. Phys. (Paris) **47**, 263.

Uwaha, M., and P. Nozières, 1989, in *Proceedings of the Oji International Seminar on Morphology and Growth Unit of Crystals, Yamagata, Japan, 1985*, edited by I. Sunagawa (Terra Scientific Publishing, Tokyo), p. 17.

van Saarloos, W., and J. D. Weeks, 1995, Phys. Rev. Lett. **74**, 290.

Vekhov, Ye, and R. B. Hallock, 2012, Phys. Rev. Lett. **109**, 045303.

Weeks, J. D., and G. H. Gilmer, 1979, in *Advances in Chemical Physics*, Vol. 40, edited by I. Prigogine and S. A. Rice (Wiley InterScience, New York), p. 157.

Wilks, J., 1967, *The Properties of Liquid and Solid Helium* (Oxford University Press, New York).

Williamson, L. A., and P. B. Blakie, 2016, Phys. Rev. Lett. **116**, 025301.

Wolf, P. E., S. Balibar, and F. Gallet, 1983, Phys. Rev. Lett. **51**, 1366.

Wolf, P. E., D. O. Edwards, and S. Balibar, 1983, J. Low Temp. Phys. **51**, 489.

Wolf, P. E., F. Gallet, S. Balibar, E. Rolley, and P. Nozières, 1985, J. Phys. (Paris) **46**, 1987.

Wulff, G., 1901, Z. Kristallogr. Mineral. **34**, 449.

Xi, K. T., T. Byrnes, and H. Saito, 2018, Phys. Rev. A **97**, 023625.

Yarmchuk, E. J., M. J. V. Gordon, and R. E. Packard, 1979, Phys. Rev. Lett. **43**, 214.

Yoneyama, K., R. Nomura, and Y. Okuda, 2004, Phys. Rev. E **70**, 021606; **73**, 049901(E) (2006).

Yoshida, T., A. Tachiki, R. Nomura, and Y. Okuda, 2017, J. Phys. Soc. Jpn. **86**, 074603.

Zmeev, D. E., F. Pakpour, P. M. Walmsley, A. I. Golov, W. Guo, D. N. McKinsey, G. G. Ihas, P. V. E. McClintock, S. N. Fisher, and W. F. Vinen, 2013, Phys. Rev. Lett. **110**, 175303.

See Supplemental Material at http://link.aps.org/supplemental/10.1103/RevModPhys.92.041003 for the enlarged figure, largeFigs, and the following movie files: movieZeroG, movieFig3, movieFig4, movieFig6, movieFig8, movieFig11, movie13a, movieFig15b, movieFig15_2, movieFig18, movie19, movieFig20, movieFig23, movieFig25ab, movieFig25_2, and movieFig25_3.